composites
Part B: engineering
ScienceDirect

2-D constitutive equations for orthotropic Cosserat type laminated shells in finite element analysis

Chróścielewski Jacek, Sabik Agnieszka, Sobczyk Bartosz, Witkowski Wojciech

PII: S1359-8368(18)32512-5
DOI: https://doi.org/10.1016/j.compositesb.2018.11.101
Reference: JCOMB 6286

To appear in: *Composites Part B*

Received Date: 10 August 2018
Revised Date: 2 October 2018
Accepted Date: 25 November 2018

Please cite this article as: Jacek Chróś, Agnieszka S, Bartosz S, Wojciech W, 2-D constitutive equations for orthotropic Cosserat type laminated shells in finite element analysis, *Composites Part B* (2018), doi: https://doi.org/10.1016/j.compositesb.2018.11.101.

This is a PDF file of an unedited manuscript that has been accepted for publication. As a service to our customers we are providing this early version of the manuscript. The manuscript will undergo copyediting, typesetting, and review of the resulting proof before it is published in its final form. Please note that during the production process errors may be discovered which could affect the content, and all legal disclaimers that apply to the journal pertain.

Equation Chapter 1 Section 12-D constitutive equations for orthotropic Cosserat type laminated shells in finite element analysis

Chróścielewski Jacek (e-mail: jchrost@pg.edu.pl)
Sabik Agnieszka (e-mail: agsa@pg.edu.pl),
Sobczyk Bartosz (e-mail: barsobcz@pg.edu.pl)
Witkowski Wojciech (e-mail: wojwit@pg.edu.pl) - corresponding author
Gdansk University of Technology, Faculty of Civil and Environmental Engineering, Department of Mechanics of Materials and Structures, 80-233 Gdańsk, Narutowicza 11/12, Poland

Abstract

We propose 2-D Cosserat type orthotropic constitutive equations for laminated shells for the purpose of initial failure estimation in a laminate layer. We use nonlinear 6-parameter shell theory with asymmetric membrane strain measures and Cosserat kinematics as the framework. This theory is specially dedicated to the analysis of irregular shells, inter alia, with orthogonal intersections, since it takes into account the drilling rotation degree of freedom. Therefore, the shell is endowed naturally with 6 degrees of freedom: 3 translations and 3 rotations. The proposed equations are formulated from the statement of the generalized Cosserat plane stress with additional transverse shear components and integrated over the shell's thickness using the equivalent single layer approach (ESL). The resulting formulae are implemented into the own Fortran code enabling nonlinear shell analysis. Some numerical results are presented to show the performance of the proposed approach.

Keywords: orthotropic Cosserat, Cosserat laminates, characteristic length, drilling rotation DOF, irregular shells

Glossary of key notations

$\sigma_{aa},\sigma_{bb},\sigma_{ab},\sigma_{ba}$ - asymmetric membrane stresses in shell layer (*k*)
σ_a,σ_b - transverse shear stresses in shell layer (*k*)
m_a,m_b - Cosserat coupling moments in shell layer (*k*)
$\boldsymbol{\varepsilon}$, $\mathbf{s}$ - shell strain and shell stress vector
$\mathbf{e}$, $\boldsymbol{\sigma}$ - local strain and stress vector in shell layer
E_a, E_b - Young moduli in *a* and *b* directions of layer (*k*)
ν_{ab} - Poisson ratio of layer (*k*)
G_{ab}, G_{ac}, G_{bc} - shear moduli in *a-b, a-c, b-c* planes of layer (*k*)
G_C - Cosserat shear modulus in *a-b* plane of layer (*k*)
N - Cosserat coupling number
l_c - characteristic length of Cosserat continuum
α_s - shear correction factor
α_t - drilling stiffness correction factor
h,H - thickness of the layer (*k*) and the shell, respectively
FFt - fiber tension failure index
FFc - fiber compression failure index
FMt - matrix tension failure index
FMc - matrix compression failure index
FPF – first ply failure
NLF1 –number of shell layers with at least one failure mechanism

Introduction

Application of laminated composites as the structural material is today very common. In turn, it is a very good alternative to the use of steel, concrete or other ordinary ones in civil engineering. A lot of research is done to find the best approaches and solutions for the understanding and description of the composites behavior. New theoretical methods of analysis of laminated composites are still formulated, developed or evaluated. Some selected recent papers in this field are [1][2][3][4][5][6][7][8][9][10]. Experiments are conducted at the same time, as they are inevitable to validate the new theories or to check the performance of novel structures or their elements. The results of selected latest achievement in this area are for instance available in [11][12][13][14][15][16]. An important aspect to focus on, regarding analysis and design of laminated composites, is their initial failure or progressive damage. Although some methods and approaches have been already validated and evaluated, for instance during the World Wide Failure Exercises, see for example [17][18][19], efforts are made to analyze new modern methodologies or modify the existing ones [20][21][22][23][24][25][26][27].

In our paper we follow the aforesaid directions of research. We focus on the proper description of the material law in the geometrically nonlinear analysis of laminated shells. For this purpose we use the nonlinear 6-parameter (6p) shell theory [28][29]. The 6p theory is specially dedicated to the analysis of geometrically irregular shells, with emphasis on orthogonal intersections, as it takes into account the drilling rotation degree of freedom. It is chosen here, because a lot of structures made of laminated composites have intersections and proper descriptions of their behavior are desirable.

Our aim is also to estimate the initial failure in a laminate layer with aid of the new material law. The estimation of initial failure, also named as the First Ply Failure (FPF) method is of great importance in the design of structures made of laminated composites. Obviously, FPF describes the onset of damage in the laminate layer, which should not appear during the life cycle of an engineering structure, due to its expected reliability and durability. Therefore, in order to enable FPF calculations for the sophisticated theory and the new material law, we propose a modification of Hashin criterion, compatible with the 6p theory.

Shell theory

The shell theory used here belongs to the class of Cosserat-type shells, see for instance [30] and has the same kinematical structure as the theory of Cosserat rods, see [31] and references given there. The governing equations, jump conditions and weak forms has been already presented by the present authors and other researchers, see for instance [32][33][34][35][36][37][38][39][40]. Following, for instance [28] and notations used in [37] we present short account of the ingredients of the theory necessary to develop the constitutive relations. We consider the shell reference surface M in the undeformed configuration. We assume, without going into technical considerations, that the open subset of the set $M\backslash(\partial M \cup \Gamma)$ is regular enough to assert the existence of the metric tensor with the components given respectively by:

$$a_{\alpha\beta} = \boldsymbol{t}^0_\alpha \cdot \boldsymbol{t}^0_\beta,\ \boldsymbol{t}^0_\beta = \boldsymbol{x},_\beta,\ \beta = 1,2 \tag{1}$$

At each point $\boldsymbol{x} \subset M$, later identified with the finite element node (Fig. 1), we assume that the base vectors $\boldsymbol{t}^0_\beta = \boldsymbol{x},_\beta,\ \beta = 1,2$ together with the normal vector

$$\boldsymbol{t}^0 \equiv \boldsymbol{t}^0_3 = \frac{\boldsymbol{t}^0_1 \times \boldsymbol{t}^0_2}{\| \boldsymbol{t}^0_1 \times \boldsymbol{t}^0_2 \|} \tag{2}$$

form rigid orthogonal triad $\boldsymbol{t}^0_i(\boldsymbol{x}),\ i = 1,2,3$ .Therefore, we have Cosserat structure at each $\boldsymbol{x} \subset M$ in the initial configuration. Motion of such structures, cf. for instance [41] or [42], is described by the vector of displacement $\boldsymbol{u}(\boldsymbol{x})$ and the proper orthogonal tensor $\boldsymbol{Q}(\boldsymbol{x}) \in SO(3)$. The current position of $\boldsymbol{x}$ and the current orientation $\boldsymbol{t}_i\,(\boldsymbol{x})$ are defined by the formulae

$$\boldsymbol{y}(\boldsymbol{x}) = \boldsymbol{x} + \boldsymbol{u}(\boldsymbol{x}),\ \boldsymbol{t}_i(\boldsymbol{x}) = \boldsymbol{Q}(\boldsymbol{x})\boldsymbol{t}^0_i(\boldsymbol{x}) \tag{3}$$

In the present approach the strain fields corresponding to (3) have the following forms

$$\boldsymbol{\varepsilon}_\beta = \boldsymbol{u},_\beta + (\mathbf{1} - \boldsymbol{Q})\boldsymbol{t}^0_\beta,\ \boldsymbol{\kappa}_\beta = \mathrm{axl}(\boldsymbol{Q},_\beta \boldsymbol{Q}^{\mathrm{T}}) \tag{4}$$

The definitions (4) are exact in a sense that they emanate from the principle of virtual work, see for instance [28][29][37]. However, as shown in [43] and references given there, a multitude of formulae exist when large strains are considered.

Fig. 1. Shell in 6-parameter theory, notation

In FEM approach the reference surface M is discretized with appropriate set of finite elements $\Pi_{(e)}$. Here we use authors' 16-node C^0 elements denoted as CAM, described for instance in [28]. Each node a of the mesh within the finite element $\Pi_{(e)}$ is defined by its position vector $\boldsymbol{x}_a$ and the triad of directors $\{\boldsymbol{t}^0_i\}_a,\ i = 1,2,3$ (more generally: within the regular area of the shell, since at given node a on the edge Γ the number of triads of directors equals to the number of intersecting regular areas). The latter are treated as the given data of the problem and are defined through five parameters assuring non-singular parameterization of proper orthogonal transformation, see e.g. [44]

$$\left\{\boldsymbol{t}^0_i(\boldsymbol{x})\right\}_a = \left\{\boldsymbol{T}_0(\boldsymbol{x})\right\}_a \mathbf{e}_i,\ \boldsymbol{T}_0 \in SO(3) \tag{5}$$

In view of $(3)_2$ the current orientation field is defined by

$$\left\{\boldsymbol{t}_i(\boldsymbol{x})\right\}_a = \left\{\boldsymbol{Q}(\boldsymbol{x})\right\}_a \left\{\boldsymbol{t}^0_i(\boldsymbol{x})\right\}_a \tag{6}$$

It follows from (6) that there is a necessity to interpolate the values of $\boldsymbol{Q}(\boldsymbol{x}) \in SO(3)$. Unlike in the case of vector-valued functions such as $(3)_1$, the direct interpolation of $SO(3)$ elements $(3)_2$ is not available. Thus we use the concept of the indirect interpolation as described in detail for instance in [45].

Constitutive relation

Moving towards particularization of constitutive relation and its further implementation we write collectively components of (4) in the vector form as

$$\boldsymbol{\varepsilon} = \{\varepsilon_{11}\ \varepsilon_{22}\ \varepsilon_{12}\ \varepsilon_{21} | \varepsilon_1\ \varepsilon_2 \| \kappa_{11}\ \kappa_{22}\ \kappa_{12}\ \kappa_{21} | \kappa_1\ \kappa_2\}^{\mathrm{T}} \text{ on } M \qquad (7)$$

and corresponding energy conjugated components of internal forces and internal couples

$$\mathbf{s} = \{N^{11} N^{22} N^{12} N^{21} | Q^1 Q^2 \| M^{11} M^{22} M^{12} M^{21} | M^1 M^2\}^T \text{ on } M \qquad (8)$$

The shell theory considered here, see e.g. [29][40], uses only 2D surface resultants ($\boldsymbol{\varepsilon}$, $\mathbf{s}$) defined on M. Let's assume that the local stress state in Cosserat type laminated shells (typical layer $M(\xi)$ defined by ξ) is given by

$$\boldsymbol{\sigma} = \{\sigma_{aa} \sigma_{bb} \sigma_{ab} \sigma_{ba} | \sigma_a \sigma_b | m_a m_b\}^T \text{ on } M(\xi) \qquad (9)$$

We propose the approach based on integration of (9) over the thickness direction $\xi \in [-h^-, +h^+]$, ($h = h^- + h^+$) to the form of the stress resultants $\mathbf{s}$ (8), see e.g. [45] , using the kinematics of the laminate layer $M(\xi)$

$$\mathbf{e} = \{\varepsilon^{aa} \varepsilon^{bb} \varepsilon^{ab} \varepsilon^{ba} | \varepsilon^a \varepsilon^b | \kappa_a \kappa_b\}^T \text{ on } M(\xi) \qquad (10)$$

The formula (10) is obtained with the use of $\boldsymbol{\varepsilon}$ (7) and (4) under the assumption of Reissner-Mindlin (RM) kinematics of the shell fiber and its form is the same as for stress resultants $\mathbf{s}$ (8), see e.g. [45]. The method has been already described, see e.g. [35]-[38], [45]. The components of (8) are required in the entire shell space of the volume of the shell-like body B, i.e. at each point $\mathbf{x}(\xi, \boldsymbol{x}) \subset B$, $\xi \in [-h^-, +h^+]$, $\boldsymbol{x} \subset M$. In the present approach we indirectly connect the components of (8) with those of (7) by the *Cosserat orthotropic relation*. Our approach is motivated by the idea presented in [46] where the authors analyzed numerically linear plane stress problems of orthotropic continuum. The constitutive relation, from the work [46], is given directly for an orthotropic layer, in contrast to approaches presented e.g. in [47][48], where matrix and inclusions are treated as isolated isotropic Cosserat materials. We extend the study from [46] to nonlinear numerical analysis of shells with finite rotations and translations. Let's assume that at the $\mathbf{x}(\xi, \boldsymbol{x}) \in M(\xi, \boldsymbol{x}) \subset B$, $\xi \in [-h^-, +h^+]$, $\boldsymbol{x} \subset M$ of the surface $M(\xi)$, see Fig. 2, there exists locally on $M(\xi)$ a generalized orthotropic plane stress state of Cosserat type in the following form

$$\begin{Bmatrix} \sigma_{aa} \\ \sigma_{bb} \\ \sigma_{ab} \\ \sigma_{ba} \\ \hline \sigma_{a} \\ \sigma_{b} \\ \hline m_a \\ m_b \end{Bmatrix} = \left[\begin{array}{cccc|cc|cc} \frac{E_a}{1-\nu_{ab}\nu_{ba}} & \frac{\nu_{ab}E_b}{1-\nu_{ab}\nu_{ba}} & 0 & 0 & 0 & 0 & 0 & 0 \\ \frac{\nu_{ba}E_a}{1-\nu_{ab}\nu_{ba}} & \frac{E_b}{1-\nu_{ab}\nu_{ba}} & 0 & 0 & 0 & 0 & 0 & 0 \\ 0 & 0 & G_{ab}+G_C & G_{ab}-G_C & 0 & 0 & 0 & 0 \\ 0 & 0 & G_{ab}-G_C & G_{ab}+G_C & 0 & 0 & 0 & 0 \\ \hline 0 & 0 & 0 & 0 & \alpha_s G_{ac} & 0 & 0 & 0 \\ 0 & 0 & 0 & 0 & 0 & \alpha_s G_{bc} & 0 & 0 \\ \hline 0 & 0 & 0 & 0 & 0 & 0 & 2G_{ab}l_c^2 & 0 \\ 0 & 0 & 0 & 0 & 0 & 0 & 0 & 2G_{ab}l_c^2 \end{array}\right] \begin{Bmatrix} \varepsilon^{aa} \\ \varepsilon^{bb} \\ \varepsilon^{ab} \\ \varepsilon^{ba} \\ \hline \varepsilon^{a} \\ \varepsilon^{b} \\ \hline \kappa_a \\ \kappa_b \end{Bmatrix} \tag{11}$$

Usual notation holds in (11) (see [49], [50]) i.e. $(E_a)_k$, $(E_b)_k$ are the Young's moduli in the direction of the reinforcement and perpendicularly to the reinforcement, respectively, $(G_{ab})_k$, $(G_{ac})_k$, $(G_{bc})_k$ are the shear moduli in $a-b$, $a-c$, $b-c$ planes and $(\nu_{ab})_k$, $(\nu_{ba})_k$ denote the Poisson's ratios such that $E_a\nu_{ba}=E_b\nu_{ab}$ (no summation); α_s is the shear correction factor.

Fig. 2. Shell-like body in 6-parameter shell theory, notation

The presence of the Cosserat structure is visible in the in-plane shear components where

$$G_C = G_{ab}\frac{N^2}{1-N^2},\ 0<N<1 \tag{12}$$

and in the drilling couple stresses where the characteristic length l_c appears. In (12) we use the Cosserat coupling number N (see for instance [51]) which is discussed later. To calculate stress and couple resultants in each layer k we follow exactly the same idea as presented in [45]. The direction of the reinforcement in layer k is denoted by angle $\theta_{(k)}$ (see Fig. 2). The transformation of (11) from $\left(\mathbf{g}_1(\xi),\mathbf{g}_2(\xi)\right)$ to $(\boldsymbol{a}_{(k)},\boldsymbol{b}_{(k)})$ system, is defined as follows:

$$\mathbf{T}_k = \left[\begin{array}{cccc|cc|cc} C^2 & S^2 & SC & SC & 0 & 0 & 0 & 0 \\ S^2 & C^2 & -SC & -SC & 0 & 0 & 0 & 0 \\ -SC & SC & C^2 & -S^2 & 0 & 0 & 0 & 0 \\ -SC & SC & -S^2 & C^2 & 0 & 0 & 0 & 0 \\ \hline 0 & 0 & 0 & 0 & C & -S & 0 & 0 \\ 0 & 0 & 0 & 0 & S & C & 0 & 0 \\ \hline 0 & 0 & 0 & 0 & 0 & 0 & C & -S \\ 0 & 0 & 0 & 0 & 0 & 0 & S & C \end{array}\right]_k,\ C=\cos(\theta_{(k)}),\ S=\sin(\theta_{(k)}) \tag{13}$$

The final structure of the constitutive relation between (7) and (8)

$$\mathbf{s} = \mathbf{C}\boldsymbol{\varepsilon} \tag{14}$$

is obtained assuming the equivalent single layer (ESL) approach and Reissner-Mindlin (RM) kinematics of the shell fiber. Specifically, the distribution of plane stress components $\sigma_{aa}, \sigma_{bb}, \sigma_{ab}, \sigma_{ba}$ in the thickness direction is assumed to be linear, whereas the transverse shear σ_a, σ_b and drilling terms m_a, m_b remain constant. Such a combination: ESL+RM is typical and was used in many papers: [11][20][27][50][52]. In this study we assume that the components of $\mathbf{C}$ are kept constant during the analysis, which however does not exclude the first ply failure (FPF) analysis that will be also presented.

Discussion of proposed equation, selection of material parameters

As it can be observed, equation (11) is dependent not only on usual material constants that can be obtained through standard laboratory tests but also on the parameters of the Cosserat medium. We assume, as in [46], that the Young's moduli, Poisson's ratios and shear moduli G_{ab}, G_{ac} and G_{bc} have the same character as in Cauchy continuum. This enables the use in (11) of exactly the same values as those reported in the literature. As far as the Cosserat parameters N and l_c are concerned the situation is more complicated. Theoretical studies e.g. [53] and experimental results presented in [42] give the range of applicability for the coupling number $0 \le N < 1$ and for the characteristic length $l_c > 0$. The order of l_c is somewhere between 0.22 mm to 5.0 mm. Nonetheless in [47] it is equal to 50 mm and in [51] the characteristic length value varies between 0 and 10^6 mm. In our approach $N = 0$ (as argued also in [36]) is not possible since it yields degenerated constitutive matrix, refer to (11), in a sense that the third and the fourth row become linearly dependent. Therefore, we assume $0 < N < 1$ as the valid range for the present formulation. Since there are no physical recommendations for the determination of the characteristic length in the analysis of shells, we assume in the used theory that this parameter is related to the shell thickness, see [36]. In [36] it is clearly shown that micropolar length is related to the drilling stiffness parameter α_t, which was used in the initially proposed constitutive law established for isotropic shells in the framework of 6p shell theory. The numerical studies presented in e.g. [29] reveal that for $\alpha_t > \sim 1$ some numerical instabilities can occur, especially in the analysis of irregular shells. Therefore the usage of $\alpha_t < \sim 1$ is suggested. The proposed constitutive law associated with the drilling rotation integrated over the shell thickness (under the assumption of constant distribution of the drilling curvatures) is analogous to that used in the case of isotropic shells. Thus, it is justified to utilize the relation between α_t and characteristic length derived in [36], stating that:

$$l_c = \sqrt{\frac{\alpha_t}{12}} H \tag{15}$$

where H is the total thickness of the shell. If we assume that $\alpha_t = 1$ is the approximate upper bound value, it follows from (15) that the limit value for characteristic length is $l_c = H/\sqrt{12}$. It has to be however stressed, that this is not a strong recommendation, since the significance of the drilling stiffness influence depends on the analyzed problem and used finite element e.g. [29]. For example in [36] the value of characteristic length based on conclusions drawn numerically can be greater than $H/\sqrt{12}$ but should not exceed the shell thickness. Moreover, it has to be emphasized that the relation (15) is valid only for $N=\sqrt{2}/2$. Therefore, it is still crucial to investigate the influence of the characteristic length. In this paper it will be examined numerically, but in contrast to the above mentioned works, this will be done on the basis of local behavior as the stress state and first ply failure onset will be studied.

To sum up, it is possible in our approach to use standard values of Young's moduli, Poisson's ratios and shear moduli G_{ab}, G_{ac} and G_{bc}. The remaining terms G_c and $l_c > 0$ are parameters that must be assumed. According to relation (12) G_c becomes a multiplier of G_{ab}.

Failure criterion

To estimate the FPF load we use the Hashin criterion. It was developed in 1980 [54]. Historically, it is a very important criterion as it was the first one where different modes of failure were distinguished, namely fiber failure in tension or compression and matrix failure in tension or compression. It is still in use although almost 40 years have passed since its formulation. The recent papers, where the criterion is utilized are for instance [55][56][57][58][59][60]. The original version of Hashin criterion makes use of symmetric stress tensor. As the material law (11) on $M(\xi)$ used by us within 6p theory includes asymmetric membrane stress measures ($\sigma_{ab} \neq \sigma_{ba}$) and drilling couple stresses ($m_a \neq m_b$) it is not possible to apply the original approach here. Therefore, we formulate its special form for the purposes of the present shell theory [35], and with respect to the law (11) for

fiber tension:

$$FFt = \left(\frac{\sigma_{aa}}{X_t}\right)^2 + \alpha_H \left(\frac{\sigma_{ab}}{S_l}\right)^2 \text{ failure when } FFt = 1 \tag{16}$$

fiber compression:

$$FFc = \left(\frac{\sigma_{aa}}{X_c}\right)^2 \text{ failure when } FFc = 1 \tag{17}$$

matrix tension

$$FMt = \left(\frac{\sigma_{bb}}{Y_t}\right)^2 + \left(\frac{\sigma_{ba}}{S_l}\right)^2 \text{ failure when } FMt = 1 \tag{18}$$

matrix compression

$$FMc = \left(\frac{\sigma_{bb}}{2S_t}\right)^2 + \left[\left(\frac{Y_c}{2S_t}\right)^2 - 1\right]\frac{\sigma_{bb}}{Y_c} + \left(\frac{\sigma_{ba}}{S_l}\right)^2 \text{ failure when } FMc = 1 \tag{19}$$

where X_t and Y_t are the (absolute) values of tensile strength in the material axes *a*, *b*, X_c and Y_c denote the absolute values of compressive strength in these axes, S_l is the shear strength in the layer plane, whereas S_t describes the transverse shear strength. The parameter α_H can vary between 0 and 1. In this paper it is set as $\alpha_H = 0$.

In the equations (16)-(19) the in-plane shear stress σ_{ab} and σ_{ba} are distinguished in comparison to the original criterion where only one (symmetric) value of in-plane shear σ_{ab} is considered. Here the σ_{ab} component is used in the fiber modes expressions, whereas the σ_{ba} is associated with the matrix mode. This stems from the mechanisms of failure and possible fracture planes to occur within a lamina and is in accordance with the issues underlying formulation of the original criterion presented in [54]. The drilling couple stresses are omitted in the modified criterion, although they are included in the law (11) and in the 2D equations of shells. This assertion is based on [61], where the authors have shown that the values of drilling couples are very small for thin isotropic elastic regular shells subjected to small strain and can be neglected. Therefore, we claim that the drilling couple stresses are very small as well and they do not contribute much to the failure. Nonetheless, they are used in the governing equations of the 6p theory to maintain its structure at the shell junctions. Such an approach is also motivated by the fact that the drilling couple strength is not obtained in the standard experimental tests conducted to establish properties of a lamina and thus is quite bothersome to determine. Finally, it is worth to mention that the modified version of Hashin criterion is similar to the one proposed in [35]. However, one has to keep in mind that a different material law was used in there thus we treat this approach as a new one.

Examples

In the following section the analysis of selected numerical examples is presented. The computations are performed with the use of the authors' finite element program. The 16 node fully integrated shell element (16FI) is employed for the purpose of discretization. The shear correction factor value, in numerical calculations, is $\alpha_s = \frac{5}{6}$ at each layer. In the first example the study of the influence of the Cosserat coupling number N on the shell response undergoing large displacements is performed, whereas in the following ones attention is paid to the impact of characteristic length l_c on the failure initiation.

1. *Semi-cylindrical shell under point load*

Stander et al. [62] proposed this benchmark problem for shell finite elements. It has become very popular both with the isotropic and the laminated material, e.g. [63][64][65][66]. Here it is used only for the validation purposes. The geometry of the shell is presented in Fig. 3 where: $L = 304.8$ mm, $R = 101.6$ mm and the total shell thickness is $H = 3$ mm. Considering the case of laminated shell, following [64], the material properties are: $E_a = 20.685$ GPa, $E_b = 5.17125$ GPa, $G_{ab} = G_{ac} = 7.956$ GPa, $G_{bc} = 1.989$ GPa, $\nu_{ab} = 0.25$. The characteristic length $l_c = 0.01H$. Two stacking sequences are considered relative to the director $\boldsymbol{t}_1^0$: [90/0/90] and [0/90/0].

Fig. 3. Semi-cylindrical shell, geometry, load and director field

Load-deflection paths of the vertical displacement of the node (a) are compared with the reference solution [64] in Fig. 4. Three values of the Cosserat coupling number N, included in equation (12), are considered: 0.4, $\sqrt{2}/2$ and 0.9. A good correspondence with reference solutions is visible. Similarly, as observed in previous work e.g. [36] the value of N does not influence the shell behavior. In the following examples it will be assumed as $\sqrt{2}/2$. Such a value assures that the in-plane shear constitutive relation is exactly the same as in the earlier works published by the authors in the area of failure analysis of laminates within the 6p theory [20][35].

Fig. 4. Semi-cylindrical shell, results

2. *Quasi-isotropic laminated quadratic plate under uniformly distributed load*

Secondly a quasi-isotropic laminated quadratic plate 600×600 mm is examined. The experimental and numerical results for this example were originally presented in [67][68]. We take the advantage that the failure data is available in the aforesaid papers and therefore we estimate the FPF occurrence here as well. The plate is fixed along all edges and is subjected to uniformly distributed load. The laminate consists of 5 layers [0°/45°/90°/–45°/0°] made of glass/polyester composite with following parameters: $E_a = 23.6$ GPa, $E_b = 10$ GPa, $G_{ab} = 1$ GPa, $\nu_{ab} = 0.23$, $X_t = 735$ MPa, $X_c = 600$ MPa, $Y_t = 45$ MPa, $Y_c = 100$ MPa, $S_L = 45$ MPa. The fiber angles are measured with respect to the *x*–axis, see Fig. 5. The total thickness of the plate is $H = 3.43$ mm. The value of the transverse shear strength is taken as $S_t = 0.5\, Y_c$ [69].

Fig. 5. Quasi-isotropic plate under uniformly distributed load

As stated previously the value $N=\sqrt{2}/2$ is used for the computation. In the following examples the influence of characteristic length value l_c is examined with the justification, that this factor can be crucial in the future studies concerning the progressive failure analysis. However, in the present work only the failure initiation is investigated.

In order to provide mesh density comparable to the one from study [67], the mesh of 8×8 CAM FI elements is used in the current computations. The solution is sought with the use of the displacement control technique whereas the central deflection $w_{(a)}$ is the control parameter.

Fig. 6 presents the results for three values of characteristic length: $l_c=0$, $l_c=h$ and $l_c=H$ where h stands for the thickness of a single layer (h_k) and H is the total thickness of the plate $H=\sum_k h_k$. It can be observed that the paths obtained for different values of characteristic length coincide with each other. The FPF occurs in all the cases for $w=10.8$ mm. This value agrees with that given in [20] and corresponds well to the reference value $w=10.64$ mm reported in [67].

For the comparison purposes Fig. 6 depicts the present results together with the experimental and numerical solution given in [67]. It has to be noticed, that in [67] progressive failure analysis (PFA) was performed, therefore the agreement between that solution and the present one after the FPF onset should not be alleged. On the other hand the unexpected disagreement between the present and reference numerical solutions before the FPF is pronounced. The present model seems to be more flexible than the reference one. The numerical results reported in [67] match the experimental path better. However, in the authors' opinion it can be attributed to probably by too large increment step used in the reference computations. To prove this hypothesis additional analysis was performed in Abaqus with the use of the same mesh as in [67] and load control method. Fig. 6 illustrates the obtained results. Two solution cases are shown: "Abaqus large step (a)" and "Abaqus small step (b)". It can be seen, that in the case of "b" the solution is similar to the path obtained with the use of the authors' own program. For the "a" solution the path appears near the one for the numerical results shown in [67].

Quite apart from these discrepancies, as stated previously, the prediction of the FPF onset is very similar for the present and reference solution. Basing on the authors' earlier experience, see [20], the same conclusion concerns also the further progressive failure analysis.

Fig. 7 shows the distribution of NLF1 parameter at the failure occurrence. This parameter is defined as the number of layers in which at least one failure mechanism is detected. Due to the smoothing techniques performed by the postprocessor the values are not integer. Basing on some other postprocess data it can be verified, that the FPF is associated with the matrix cracking in the bottom layer.

Fig. 6. Quasi-isotropic plate, equilibrium paths of the central deflection

Fig. 7. Quasi-isotropic plate, first ply failure (matrix cracking in the bottom layer)

Lastly we analyze the significance of the influence of the coupling stresses on the local response of the plate. As stated earlier these stresses are omitted in the failure criterion and it is crucial to check, whether such an assumption is justified. The coupling stresses are nonlinearly dependent on the characteristic length value. It is essential to compare the impact of coupling and force stresses on the failure indices. For such a comparison the ratios m_a / l_c and m_b / l_c are taken into account, since they yield the values measured in units of force stresses. The following study is made for two analyzed characteristic lengths ($l_c = h$ and $l_c = H$): firstly the Gauss point where the FPF onset arises is identified and the failure indices *FF*, *FM* in this point and the values of the corresponding stress components are given; secondly the Gauss points where ratios m_a / l_c and m_b / l_c approach the extreme values are found and then their behavior together with failure indices *FF*, *FM* are presented. It has to be emphasized that in the course of the analysis the points where m_a / l_c and m_b / l_c as well as the indices *FF*, *FM* reach the extreme levels change the location. Therefore, in the following figures the shown paths cannot be presented in the entire range of the assumed control displacement. The displayed displacement range includes the instance of the FPF onset.

Fig. 8 and Fig. 9 depict the growth of failure indices and the corresponding stress components at the failure point for $l_c = h$. From these figures it is clear that the failure is due to the matrix tension for $w = 10.8$ mm. Fiber failure does not play a role in this example. Fig. 9 proves explicitly that the σ_{bb} stress component has the strongest influence on the *FM* index . The stresses σ_{ba} as well as the coupling stresses are significantly lower.

Fig. 8. Failure indices progress in the FPF localization (*x*=305 mm, *y*=595 mm, layer 1), l_c=*h*

Fig. 9. Stress components response in the failure point (*x*=305 mm, *y*=595 mm, layer 1), l_c=*h*

Fig. 10 and Fig. 11 illustrate the changes of maximum m_a / l_c and m_b / l_c ratios and corresponding failure indices in respective Gauss points. It is observed in Fig. 10 that in the point of maximum m_a / l_c value the stress safety margin is high, since both failure indices are very low. On the other hand, Fig. 11 shows that in the point of extreme m_b / l_c ratio the matrix cracking occurs for $w = 11.3$ mm. It is very close to the identified FPF onset value for $w = 10.8$ mm. However, the value of m_b / l_c is still evidently small and it can be assumed that it would not have significant influence on the failure behavior.

Fig. 10. Maximum m_a/l_c ratio and corresponding failure indices (x=380 mm, y=521 mm, layer 3), $l_c=h$

Fig. 11. Maximum m_b/l_c ratio and corresponding failure indices (x=220 mm, y=595 mm, layer 1), $l_c=h$

Similar conclusions can be drawn with respect to the results obtained for $l_c = H$, see Fig. 12, Fig. 13, Fig. 14 and Fig. 15. Obviously, the ratios m_a / l_c and m_b / l_c are in this case higher due to the larger characteristic length value. Nonetheless, they are still very small. Taking into account that the failure criteria include the square of stress components, the obtained results seem to prove that the assumption of small coupling stresses is in this example fully justified.

Fig. 12. Failure indices progress in the FPF localization (x=305 mm, y=595 mm, layer 1), $l_c=H$

Fig. 13. Stress components response in the failure point (x=305 mm, y=595 mm, layer 1), $l_c=H$

Fig. 14. Maximum m_a/l_c ratio and corresponding failure indices (x=220 mm, y=595 mm, layer 3), $l_c=H$

Fig. 15. Maximum m_b/l_c ratio and corresponding failure indices (x=220 mm, y=595 mm, layer 1), $l_c=H$

3. Axially compressed flat panel

As a next example we analyze the failure initiation in the axially compressed flat panel. This one has been widely examined, see e.g. [50][70][71][72]. It has to be noticed that the geometrical and material data are slightly different depending on the literature source. For the sake of clarity it has to be stressed, that in this paper the data is taken after [70]. The panel is 508 mm long and 178 mm wide (Fig. 16). The shorter edges are clamped, whereas the loaded one is free to translate in the axial direction. The longer edges are simply supported. T300/5208 graphite-epoxy composite which the layers are made of, is characterized by the following parameters: E_a = 131 GPa, E_b = 13.03 GPa, $G_{ab} = G_{ac}$ = 6.205 GPa, G_{bc} = 3.447 GPa, ν_{ab} = 0.38, X_t = 1379 MPa, X_c = 1137 MPa, Y_t = 81 MPa, Y_c = 189 MPa, S_L = 62 MPa. The value of the transverse shear strength is taken as previously, i.e. S_t = 0.5 Y_c. The stacking sequence of 0.132 mm thick layers h is $[45°/–45°/0°/0°/45°/–45°/0°/0°/45°/–45°/0°/90°]_s$, whereas the orientation angle is measured in reference to the axial direction. The mesh of 24×16 elements 16FI is used in the discretization process. In order to enforce the two half-waves buckling shape in the computations additional small perturbation forces $P_i = 0.00005P$ are applied (Fig. 16). The axial displacement u of the loaded edge is taken as the path control parameter. All nodes along this edges are kinematically coupled as regard the axial translation. The definition of boundary conditions is noteworthy. The description ‘clamped edge’ is clear, however, ‘simply supported’ or ‘knife edge’ (see [70]) is not obvious (compare e.g. [50][71]) especially regarding the drilling rotation.

In the present study the simply supported edge is understood as the following condition: $w = \varphi_y = 0$ (Fig. 16).

Fig. 16. Axially compressed flat panel

Fig. 17 depicts the obtained equilibrium paths of the axial displacements obtained for three values of characteristic length ($l_c = 0$, $l_c = h$, $l_c = H$) together with the reference solution given in [70], where progressive failure analysis was carried out. The Cosserat coupling number N is set to $\sqrt{2}/2$.

Fig. 17. Axially compressed flat panel – equilibrium paths of the axial displacement

It can be observed, that the characteristic length l_c does not influence significantly the global structure behavior. For all the values of characteristic length l_c the FPF onset is detected at $u = 2.03$ mm which corresponds to $P = 87720$ N. Fig. 18 illustrates distribution of the NLF1 coefficient at the FPF onset. The failure is due to the matrix cracking. The laminate fails in 0° oriented layers (layer 3 and 22). In contrast, the Hashin criterion estimation failure initiates, according to paper [72], in the third bottom layer for $P = 85500$ N. This is only in some extent lower than the present one. This small discrepancy follows from different Gauss point distribution in the thickness direction: in the present study the failure stress is controlled only in the middle of each layer, whereas in [72] in the middle and at the top and at bottom faces.

Fig. 18. FPF location in the buckled panel for two types of boundary conditions

Unfortunately, in [70] the failure initiation value was not investigated. On the other hand in [71] some report in this field is given and the FPF load equals $P = 82800$ N, according to the Christensen's criterion and $P = 96873$ N, according to the Hashin criterion. The experimental data is inopportunely not available. It has to be however emphasized that in [71] slightly different set of geometrical data was used in the computations, so that the discrepancy between these results and the present ones is rather obvious.

Fig. 19 to Fig. 26 present a similar study, as made in the previous example, of the impact of coupling moments on the stress state and FPF onset. Contrary to the previous example in this case the membrane stresses are much more pronounced. In effect it is expected, that the values of drilling moments will be more noticeable. Fig. 19, Fig. 20, Fig. 23 and Fig. 24 illustrate that the failure is caused by the matrix cracking (18). it follows from Fig. 20 and Fig. 24 that the σ_{ba} stress component has the biggest contribution to the failure condition (18). In the case of $l_c = h$ the drilling moments are evidently negligible (Fig. 20), whereas for $l_c = H$ the m_a / l_c ratio is of the same range as σ_{bb} (Fig. 24). However, the authors presume that the condition for matrix failure should rather include the m_b / l_c ratio, which is markedly small in the failure zone in this example, even for $l_c = H$. The ratio m_a / l_c ought to be considered for the fiber failure index which is in turn noticeably small in the FPF region.

Fig. 21, Fig. 22, Fig. 25 and Fig. 26 depict the maximum m_a / l_c and m_b / l_c ratios at relevant Gauss points together with the corresponding failure indices. It can be observed, that quite large drilling moments arise in the corners of the plate for $l_c = H$ (Fig. 25, Fig. 26). For $l_c = h$ these values are rather small. Nonetheless, the corresponding failure indices for both characteristic lengths are remarkably small.

The example shows that even for large values of the drilling moments the assumption of their absence in the failure criterion is reasonable here.

Fig. 19. Failure indices progress in the FPF localization (x=247 mm, y=3.67 mm, layer 3), l_c=h

Fig. 20. Stress components response in the failure point (x=247 mm, y=3.67 mm, layer 3), l_c=h

Fig. 21. Maximum m_a/l_c ratio and corresponding failure indices (x=1.47 mm, y=0.77 mm, layer 3), l_c=h

Fig. 22. Maximum m_b/l_c ratio and corresponding failure indices (x=1.47 mm, y=0.77 mm, layer 12), l_c=h

Fig. 23. Failure indices progress in the FPF localization (x=255 mm, y=177 mm, layer 22), l_c=H

Fig. 24. Stress components response in the failure point (x=255 mm, y=177 mm, layer 22), l_c=H

Fig. 25. Maximum m_a/l_c ratio and corresponding failure indices (x=1.47 mm, y=0.77 mm, layer 3), l_c=H

Fig. 26. Maximum m_b/l_c ratio and corresponding failure indices (x=1.47 mm, y=0.77 mm, layer 12), l_c=H

4. Axially compressed channel-section column

An axially compressed channel-section column is analyzed following [73]. The geometrical data is given in Fig. 27. The column is made of GFRP 8-layer laminate oriented according to the scheme

[0°/–45°/+45°/90°]$_s$, whereas the orientation angle is measured with the reference to the *y*–axis (Fig. 27). Each layer is 0.26 mm thick and possesses the following stiffness and strength properties: E_a = 38.5 GPa, E_b = 8.1 GPa, G_{ab} = 2 GPa, ν_{ab} = 0.27, X_t = 792 MPa, X_c = 679 MPa, Y_t = 39 MPa, Y_c = 71 MPa, S_L = 108 MPa. In the experiment the structure was placed between stiff plates. The loaded top plate was free to move only in the vertical direction. According to [73] the flanges of the column undergo buckling into two half waves along the height. To enforce corresponding buckling mode in the present FEM computations small perturbation forces $P_i = 0.002P$ are applied, see Fig. 27. The boundary conditions in the FEM analysis, in the source paper [73], were imposed as simply supported whereas the translations along the C-contour were left free. In this study, basing on the authors' earlier experience [20], the top edges are modelled as clamped with the possible motion in the axial direction and the bottom edges are assumed as pinned. The axial displacement of the top edge is chosen as the solution control parameter. All the nodes along this top edge are kinematically coupled with respect to the vertical translation. In the computations regular mesh of 16 FI elements is used: 30 elements along the column's height, 6 elements along the width of flanges and 12 elements along the web's width.

The results obtained for $N = \sqrt{2}/2$ and three values of characteristic lengths are shown in Fig. 28. For comparison purposes also the FEM solution given in [73] is presented. It can be seen that the present postbuckling paths do not match exactly the results from [73]. Additional analyses, though not presented here, lead to the conclusion that this is attributed to different boundary conditions in both models.

It follows from the comparison of the obtained equilibrium paths that the change of characteristic length does not influence the overall shell behavior. The local response is also very similar in all performed computations. The FPF for each chosen characteristic length value takes place for $v = 0.88$ mm. This value agrees with the result obtained in [20] and [73]. The cracking of matrix is the first damage to be observed and occurs in the outer layer in the local dimple of the web, see Fig. 29.

Fig. 27. Channel-section – scheme of the experimental setup and FEM model

Fig. 28. Channel-section column – equilibrium paths of the vertical translation

Fig. 29. Channel-section column – location of the FPF onset

Fig. 30 to Fig. 37 present the influence of the drilling moment on the stress state. It follows from Fig. 30, Fig. 31, Fig. 34, Fig. 35 that the failure arises at $v = 0.88$ mm due to the matrix cracking. The dominating stress component according to the condition (18) is σ_{bb}. The in-plane shear components as well as the drilling moments, see Fig. 31 and

Fig. 35, are negligible. Fig. 32, Fig. 33, Fig. 36 and Fig. 37 illustrate the changes of ratios m_a / l_c and m_b / l_c compared with failure indices in Gauss points in which the drilling moments attain extreme levels. In this example the points in which the couple stresses reach the maximum values do not change their position above the control displacement equal to $v \approx 0.3$ for $l_c = h$ and $v \approx 0.8$ for $l_c = H$. Therefore relatively large range of the m_a / l_c and m_b / l_c curves can be displayed. The extreme values of drilling moments for both characteristic lengths arise close to the walls intersection of the column. Similarly, as in the case of previously analyzed compressed plate, the values of m_a / l_c and m_b / l_c ratios are more pronounced than in the case of the plate undergoing bending. Nevertheless, at the moment of the FPF ($v = 0.88$) the failure indices near to the walls junction are considerably less than one. It proves that the usage of failure conditions neglecting the drilling moments is in this example correct.

Fig. 30. Failure indices progress in the FPF localization (x=-39.5 mm, y=58.9 mm, z=0 mm layer 8), l_c=h

Fig. 31. Stress components response in the failure point (x=-39.5 mm, y=58.9 mm, z=0 mm layer 8), l_c=h

Fig. 32. Maximum m_a/l_c ratio and corresponding failure indices (x=-80 mm, y=0.579 mm, z=-0.463 mm, layer 4), l_c=h

Fig. 33. Maximum m_b/l_c ratio and corresponding failure indices (x=-80 mm, y=0.579 mm, z=-0.463 mm, layer 1), l_c=h

Fig. 34. Failure indices progress in the FPF localization (x=-39.5 mm, y=58.9 mm, z=0 mm layer 8), l_c=H

Fig. 35. Stress components response in the failure point (x=-39.5 mm, y=58.9 mm, z=0 mm layer 8), l_c=H

Fig. 36. Maximum m_a/l_c ratio and corresponding failure indices (x=-80 mm, y=0.579 mm, z=-0.463 mm, layer 4), l_c=H

Fig. 37. Maximum m_b/l_c ratio and corresponding failure indices (x=-80 mm, y=0.579 mm, z=-0.463 mm, layer 1), $l_c=H$

Conclusions

2-D constitutive law for orthotropic Cosserat type laminated shells is proposed. In contrary to previous authors' works concerning laminates the presented relation utilizes 5 engineering constants and 2 additional parameters typical for Cosserat medium, namely the Cosserat coupling number N and characteristic length l_c. Since the experimental determination of these constants is not a trivial task it is essential to study their influence numerically. In this work numerical tests are performed regarding the geometrically non-linear behavior and failure initiation (FPF). Firstly, the influence of N is studied. It is shown, that the Cosserat coupling number ranging between 0.4 and 0.9 does not influence the overall response of the structure. Therefore, in further examples $N=\sqrt{2}/2$ is assumed, asserting that the in-plane shear relation is the same as in the previous authors research and the influence of characteristic length is analyzed. This constant seems to be crucial from view of the future progressive failure analysis, as it can serve as a regularization parameter. At this stage, however, only the FPF onset is studied by making use of the Hashin criterion, formulated taking into account the asymmetry of in-plane shear stresses and neglecting the drilling moments. It is shown that the value of characteristic length varying between 0 and shell thickness does not influence significantly the global behavior of the structure. Obviously, the drilling moments increase nonlinearly with the growth of the characteristic length. Their contribution is more pronounced if the membrane stress state is present. Nonetheless, it is shown on the basis of the analyzed examples that they have no impact on the FPF onset, even for large values of l_c.

Basing on the obtained results from numerical calculations a conclusion can be drawn. If the stiffness associated with the drilling moment is small, which corresponds to small values of characteristic length $l_c < H$ or, all the more so, as used in the previous research to the parameter $\alpha_t < 1$, the omission of couple stresses in the failure criterion is fully justified. However, if l_c reaches the value of shell's thickness (or larger), it is recommended to check the stress safety margin in the zones of extreme drilling moments, especially if the membrane stresses are noticeable. At this stage of the research, it remains an open question whether the modified failure criterion taking into account the couple stresses should be used for larger values of characteristic length. The study of this topic is planned to be done in the near future. Additionally, progressive failure analysis is planned to be accounted for. Some preliminary results can be found in [74].

Acknowledgements

The authors acknowledge financial support from the grant No UMO 2015/17/B/ST8/02190, financed by National Science Centre Poland.

Literature

[1] Singh DB, Singh BN. New higher order shear deformation theories for free vibration and buckling analysis of laminated and braided composite plates. Int J Mech Sci 2017;131–132:265–77. doi:10.1016/j.ijmecsci.2017.06.053.

[2] Pagani A, Carrera E. Large-deflection and post-buckling analyses of laminated composite beams by Carrera Unified Formulation. Compos Struct 2017;170:40–52. doi:10.1016/j.compstruct.2017.03.008.

[3] Teter A, Mania RJ, Kolakowski Z. Non-linear stability and load-carrying capacity of thin-walled laminated columns in aspects of coupled buckling and coupled stiffness submatrix. Compos Struct 2018;192:72–81. doi:10.1016/j.compstruct.2018.02.070.

[4] Hasim KA. Isogeometric static analysis of laminated composite plane beams by using refined zigzag theory. Compos Struct 2018;186:365–74. doi:10.1016/j.compstruct.2017.12.033.

[5] Ou X, Zhang X, Zhang R, Yao X, Han Q. Weak form quadrature element analysis on nonlinear bifurcation and post-buckling of cylindrical composite laminates. Compos Struct 2018;188:266–77. doi:10.1016/j.compstruct.2018.01.007.

[6] Wan L, Yang D, Ismail Y, Sheng Y. 3D particle models for composite laminates with anisotropic elasticity. Compos Part B Eng 2018;149:110–21. doi:10.1016/j.compositesb.2018.05.022.

[7] Liao BB, Jia LY. Finite element analysis of dynamic responses of composite pressure vessels under low velocity impact by using a three-dimensional laminated media model. Thin-Walled Struct 2018;129:488–501. doi:10.1016/j.tws.2018.04.023.

[8] Arruda MRT, Garrido M, Castro LM., Ferreira AJM, Correia JR. Numerical modelling of the creep behaviour of GFRP sandwich panels using the Carrera Unified Formulation and Composite Creep Modelling. Compos Struct 2018;183:103–13. doi:10.1016/j.compstruct.2017.01.074.

[9] Tornabene F, Fantuzzi N, Bacciocchi M. Free vibrations of free-form doubly-curved shells made of functionally graded materials using higher-order equivalent single layer theories. Compos Part B Eng 2014;67:490–509. doi:10.1016/j.compositesb.2014.08.012.

[10] Fazzolari FA. Reissner’s Mixed Variational Theorem and variable kinematics in the modelling of laminated composite and FGM doubly-curved shells. Compos Part B Eng 2016;89:408–23. doi:10.1016/j.compositesb.2015.11.031.

[11] Chróścielewski J, Miśkiewicz M, Pyrzowski Ł, Sobczyk B, Wilde K. A novel sandwich footbridge - Practical application of laminated composites in bridge design and in situ measurements of static response. Compos Part B Eng 2017;126:153–61. doi:10.1016/j.compositesb.2017.06.009.

[12] Chróścielewski J, Miśkiewicz M, Pyrzowski Ł, Rucka M, Sobczyk B, Wilde K. Modal properties identification of a novel sandwich footbridge – Comparison of measured

dynamic response and FEA. Compos Part B Eng 2018. doi:10.1016/j.compositesb.2018.06.016.

[13] Yademellat H, Nikbakht A, Saghafi H, Sadighi M. Experimental and numerical investigation of low velocity impact on electrospun nanofiber modified composite laminates. Compos Struct 2018;200:507–14. doi:10.1016/j.compstruct.2018.05.146.

[14] Li Y, Pimenta S, Singgih J, Nothdurfter S, Schuffenhauer K. Experimental investigation of randomly-oriented tow-based discontinuous composites and their equivalent laminates. Compos Part A Appl Sci Manuf 2017;102:64–75. doi:10.1016/j.compositesa.2017.06.031.

[15] Kharghani N, Guedes Soares C. Experimental, numerical and analytical study of bending of rectangular composite laminates. Eur J Mech - A/Solids 2018;72:155–74. doi:10.1016/j.euromechsol.2018.05.007.

[16] Tan W, Naya F, Yang L, Chang T, Falzon BG, Zhan L, et al. The role of interfacial properties on the intralaminar and interlaminar damage behaviour of unidirectional composite laminates: Experimental characterization and multiscale modelling. Compos Part B Eng 2018;138:206–21. doi:10.1016/j.compositesb.2017.11.043.

[17] Kaddour AS, Hinton MJ, Soden PD. A comparison of the predictive capabilities of current failure theories for composite laminates: additional contributions. Compos Sci Technol 2004;64:449–76. doi:10.1016/S0266-3538(03)00226-4.

[18] Hinton M., Kaddour A., Soden P. A further assessment of the predictive capabilities of current failure theories for composite laminates: comparison with experimental evidence. Compos Sci Technol 2004;64:549–88. doi:10.1016/S0266-3538(03)00227-6.

[19] Soden P., Kaddour A., Hinton M. Recommendations for designers and researchers resulting from the world-wide failure exercise. Compos Sci Technol 2004;64:589–604. doi:10.1016/S0266-3538(03)00228-8.

[20] Sabik A. Progressive failure analysis of laminates in the framework of 6-field non-linear shell theory. Compos Struct 2018; 200: 195-203.

[21] Koh R, Madsen B. Strength failure criteria analysis for a flax fibre reinforced composite. Mech Mater 2018;124:26–32. doi:10.1016/j.mechmat.2018.05.005.

[22] Gu J, Chen P. Some modifications of Hashin’s failure criteria for unidirectional composite materials. Compos Struct 2017;182:143–52. doi:10.1016/j.compstruct.2017.09.011.

[23] Thomson DM, Cui H, Erice B, Hoffmann J, Wiegand J, Petrinic N. Experimental and numerical study of strain-rate effects on the IFF fracture angle using a new efficient implementation of Puck’s criterion. Compos Struct 2017;181:325–35. doi:10.1016/j.compstruct.2017.08.084.

[24] Gu J, Chen P. Extension of Puck’s inter fibre fracture (IFF) criteria for UD composites. Compos Sci Technol 2018;162:79–85. doi:10.1016/j.compscitech.2018.04.019.

[25] Obert E, Daghia F, Ladevèze P, Ballere L. Micro and meso modeling of woven composites: Transverse cracking kinetics and homogenization. Compos Struct 2014;117:212–21. doi:10.1016/j.compstruct.2014.06.035.

[26] Wang B, Fang G, Liu S, Fu M, Liang J. Progressive damage analysis of 3D braided composites using FFT-based method. Compos Struct 2018;192:255–63. doi:10.1016/j.compstruct.2018.02.040.

[27] Rozylo P, Debski H, Kubiak T. A model of low-velocity impact damage of composite plates subjected to Compression-After-Impact (CAI) testing. Compos Struct 2017;181:158–70. doi:10.1016/j.compstruct.2017.08.097.

[28] Chróścielewski J, Makowski J, Stumpf H. Genuinely resultant shell finite elements accounting for geometric and material non-linearity. Int J Numer Meth Eng 1992; 35: 63–94.

[29] Chróścielewski J, Makowski J, Stumpf H. Finite element analysis of smooth, folded and multi-shell structures. Comp. Meth. Appl. Mech. Engng 1997; 141: 1–46.

[30] Altenbach J, Altenbach H, Eremeyev VA. On generalized Cosserat-type theories of plates and shells: a short review and bibliography. Archive of Applied Mechanics, 2010;80:73-92.

[31] Miśkiewicz M. Structural response of existing spatial truss roof construction based on Cosserat rod theory. Contin Mech Thermodyn 2018. doi:10.1007/s00161-018-0660-8.

[32] Altenbach H, Eremeyev VA. Actual developments in the nonlinear shell theory—state of the art and new applications of the six-parameter shell theory. Shell structures: Theory and applications vol. 3, 2014:3–12.

[33] Eremeyev VA, Lebedev LP, Cloud MJ. The Rayleigh and Courant variational principles in the six-parameter shell theory. Mathematics and Mechanics of Solids, 2015; 20(7): 806–822.

[34] Bîrsan M, Neff P. Existence of minimizers in the geometrically non-linear 6-parameter resultant shell theory with drilling rotations, Mathematics and Mechanics of Solids 2014;19(4):376–397.

[35] Chróścielewski J, Sabik A, Sobczyk B, Witkowski W. Nonlinear FEM 2D failure onset prediction of composite shells based on 6-parameter shell theory. Thin-Walled Struct 2016;105:207–19.

[36] Burzyński S, Chróścielewski J, Witkowski W. Geometrically nonlinear FEM analysis of 6-parameter resultant shell theory based on 2-D Cosserat constitutive model. ZAMM - J Appl Math Mech 2016;96:191–204.

[37] Burzyński S, Chróścielewski J, Daszkiewicz K, Witkowski W. Geometrically nonlinear FEM analysis of FGM shells based on neutral physical surface approach in 6-parameter shell theory. Compos Part B Eng 2016;107:203–13.

[38] Burzyński S, Chróścielewski J, Daszkiewicz K, Witkowski W. Elastoplastic nonlinear FEM analysis of FGM shells of Cosserat type. Compos Part B Eng 2018. doi:10.1016/j.compositesb.2018.07.055.

[39] Eremeyev VA, Pietraszkiewicz W. Local symmetry group in the general theory of elastic shells. Journal of Elasticity 2006;85(2):125–152.

[40] Libai A, Simmonds JG. The Nonlinear Theory of Elastic Shells, 2nd ed. 1998, Cambridge University Press, Cambridge

[41] Toupin RA. Theories of Elasticity with Couple-stress, Archive for Rational Mechanics and Analysis 1964;17(2):85–112.

[42] Eremeyev VA, Lebedev LP, Altenbach H. Foundations of Micropolar Mechanics, 2013, Springer.

[43] Pietraszkiewicz W. Eremeyev VA, On vectorially parameterized natural strain measures of the non-linear Cosserat continuum. International Journal of Solids and Structures, 2009;46(11):2477-2480

[44] Stuelpnagel J. On the parameterization of the three-dimensional rotation group. SIAM Review 1964;6:422–430.

[45] Chróścielewski J, Kreja I, Sabik A, Witkowski W. Modeling of composite shells in 6-parameter nonlinear theory with drilling degree of freedom, Mech. Adv. Mater. Struct. 2011;18:403–419.

[46] Nakamura S, Benedict R, Lakes R. Finite element method for orthotropic micropolar elasticity. Int. J. Engng. Sci. Eng. 1984;22:319-330.

[47] Fantuzzi N, Leonetti L, Trovalusci P, Tornabene F. Some Novel Numerical Applications of Cosserat Continua. International Journal of Computational Methods 2018; Vol. 15, No. 3, 1850054 (38 pages).

[48] Tornabene F, Fantuzzi N, Bacciocchi M. Mechanical behaviour of composite Cosserat solids in elastic problems with holes and discontinuities. Composite Structures 2017; 179:468-481.

[49] Kaw AK. Mechanics of Composite Materials, Second edition. Boca Raton, London, New York: Taylor & Francis Group; 2006.

[50] Reddy JN. Mechanics of laminated composite plates and shells. Theory and analysis. 2th edition. 2004, CRC Press.

[51] Jeong J, Ramezani H, Münch I, Neff P. A numerical study for linear isotropic Cosserat elasticity with conformally invariant curvature, Z. Angew. Math. Mech. 2009;89(7):552 – 569 (2009)

[52] Li X, Yu K, Han J, Song H, Zhao R. Buckling and vibro-acoustic response of the clamped composite laminated plate in thermal environment. Int J Mech Sci 2016;119:370–82. doi:10.1016/j.ijmecsci.2016.10.021

[53] Sander O, Neff P, Bîrsan M. Numerical treatment of a geometrically nonlinear planar Cosserat shell model, arXiv:1412.3668v1 [math.NA] 11 Dec 2014.

[54] Hashin Z. Failure Criteria for Unidirectional Fiber Composites. J Appl Mech 1980;47:329–34. doi:10.1115/1.3153664.

[55] Yuan-Sheng C. Physical interpretation of Hashin's criterion of fatigue failure under multiaxial stress. Eng Fract Mech 1986;24:165–7. doi:10.1016/0013-7944(86)90048-2.

[56] Wang FS, Yu XS, Jia SQ, Li P. Experimental and numerical study on residual strength of aircraft carbon/epoxy composite after lightning strike. Aerosp Sci Technol 2018;75:304–14. doi:10.1016/j.ast.2018.01.029.

[57] Bsisu KA-D, Hussein HH, Sargand SM. The Use of Hashin Damage Criteria, CFRP–Concrete Interface and Concrete Damage Plasticity Models in 3D Finite Element Modeling of Retrofitted Reinforced Concrete Beams with CFRP Sheets. Arab J Sci Eng 2017;42:1171–84. doi:10.1007/s13369-016-2356-3.

[58] Yu G, Ren Y, Zhang T, Xiao W, Jiang H. Hashin Failure Theory Based Damage Assessment Methodology of Composite Tidal Turbine Blades and Implications for the Blade Design. China Ocean Eng 2018;32:216–25. doi:10.1007/s13344-018-0023-z.

[59] Gu J, Chen P. Some modifications of Hashin's failure criteria for unidirectional composite materials. Compos Struct 2017;182:143–52. doi:10.1016/j.compstruct.2017.09.011.

[60] Duarte APC, Díaz Sáez A, Silvestre N. Comparative study between XFEM and Hashin damage criterion applied to failure of composites. Thin-Walled Struct 2017;115:277–88. doi:10.1016/j.tws.2017.02.020.

[61] Pietraszkiewicz W, Konopińska V. Drilling couples and refined constitutive equations in the resultant geometrically non-linear theory of elastic shells. Int J Solids Struct 2014;51:2133–43. doi:10.1016/j.ijsolstr.2014.02.022.

[62] Stander N, Matzenmiller A, Ramm E. An assessment of assumed strain methods in finite rotation shell analysis, Engineering Computations 1989;6:58–66.

[63] Klinkel S, Gruttmann F, Wagner W. A continuum based three-dimensional shell element for laminated structures, Computers and Structures 1999;71:43–62.

[64] Sze KY, Liu XH, Lo SH. Popular benchmark problems for geometric nonlinear analysis of shells, Fin. Elem. Anal. Des. 2004;40:1151–1569.

[65] Arciniega RA, Reddy JN.,Tensor-based finite element formulation for geometrically nonlinear analysis of shell structures, Comput. Methods Appl. Mech. Engrg. 2007;196: 1048–1073.

[66] Wiśniewski K. Finite Rotation Shells. Barcelona: Springer, 2010.

[67] Padhi GS, Shenoi RA, Moy SSJ, Hawkins GL. Progressive failure and ultimate collapse of laminated composite plates in bending, Compos Struct 1998; 40: 277-291.

[68] Moy SSJ, Shenoi RA, Allen HG. Strength and stiffness of fibre-reinforced plastic plates, Proc. Instn Cio Engrs Structs & Bldgs 1996; 116: 204-220.

[69] Davila CG, Camanho PP, Rose CA. Failure Criteria for FRP Laminates. J. Compos. Mater 2005; 39: 323-345.

[70] Knight NF, Rankin CC, Brogan FA. STAGS computational procedure for progressive failure analysis of laminated composite structures. International Journal of Non-linear Mechanics 2002;37: 833-849.

[71] Sleight DW. Progressive failure analysis methodology for laminated composite structures, NASA/TP-1999-209107.

[72] Sobczyk B. FEM analysis of composite materials failure in nonlinear six field shell theory, PhD thesis, Gdańsk University of Technology, 2017.

[73] Gliszczyński A, Kubiak T. Progressive failure analysis of thin-walled composite columns subjected to uniaxial compression. Composite Structures 2017;169:52-61.

[74] Chróścielewski J, Sabik A, Sobczyk B, Witkowski W. Analysis of laminates with the use of 2-D Cosserat constitutive model, 41st Solid Mechanics Conference, August 27-31, 2018 Warsaw, Poland, http://solmech2018.ippt.pan.pl/abstracts/0289.pdf

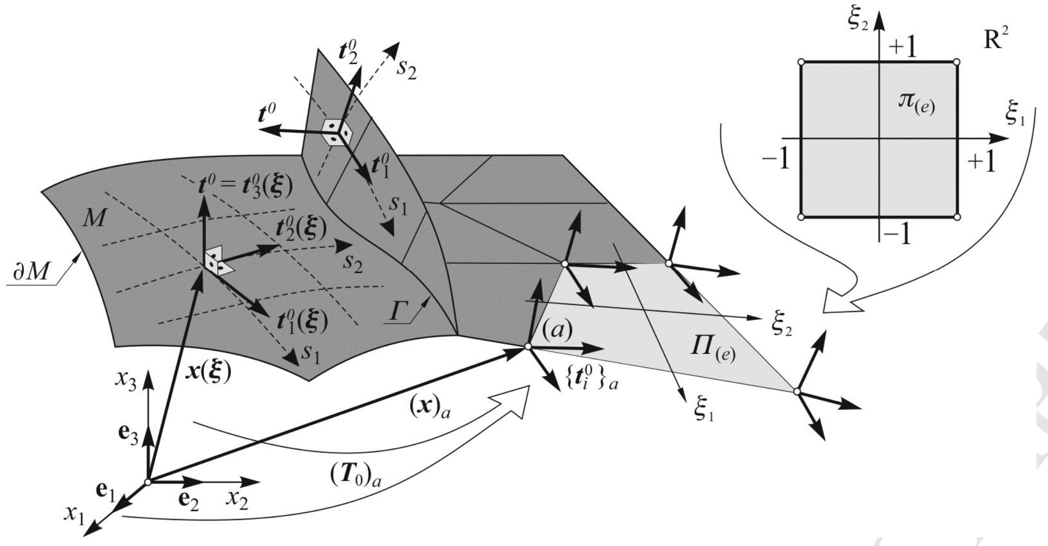
ξ_2
$+1$
R^2
$\pi_{(e)}$
ξ_1
-1
$+1$
-1
t_2^0
s_2
t^0
t_1^0
s_1
$t^0 = t_3^0(\xi)$
M
$t_2^0(\xi)$
s_2
∂M
$t_1^0(\xi)$
Γ
s_1
$x(\xi)$
(a)
ξ_2
$\Pi_{(e)}$
$\{t_i^0\}_a$
ξ_1
x_3
$\mathbf{e}_3$
$(x)_a$
$(T_0)_a$
$\mathbf{e}_1$
$\mathbf{e}_2$
x_2
x_1

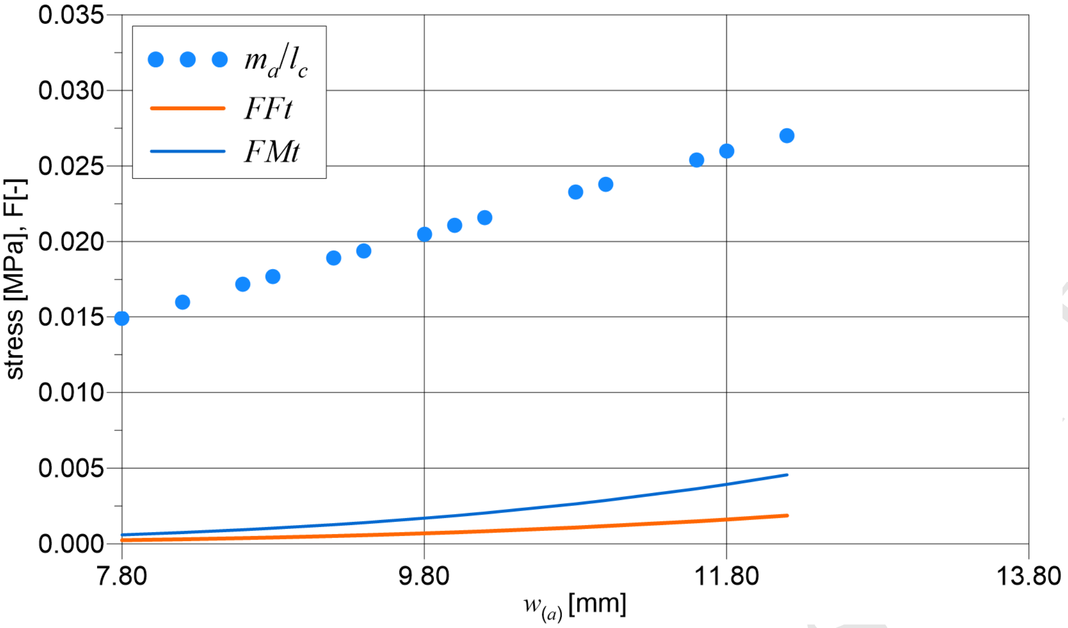
0.035
0.030
0.025
0.020
0.015
0.010
0.005
0.000
stress [MPa], F[-]
m_a/l_c
FFt
FMt
7.80
9.80
11.80
13.80
$w_{(a)}$ [mm]

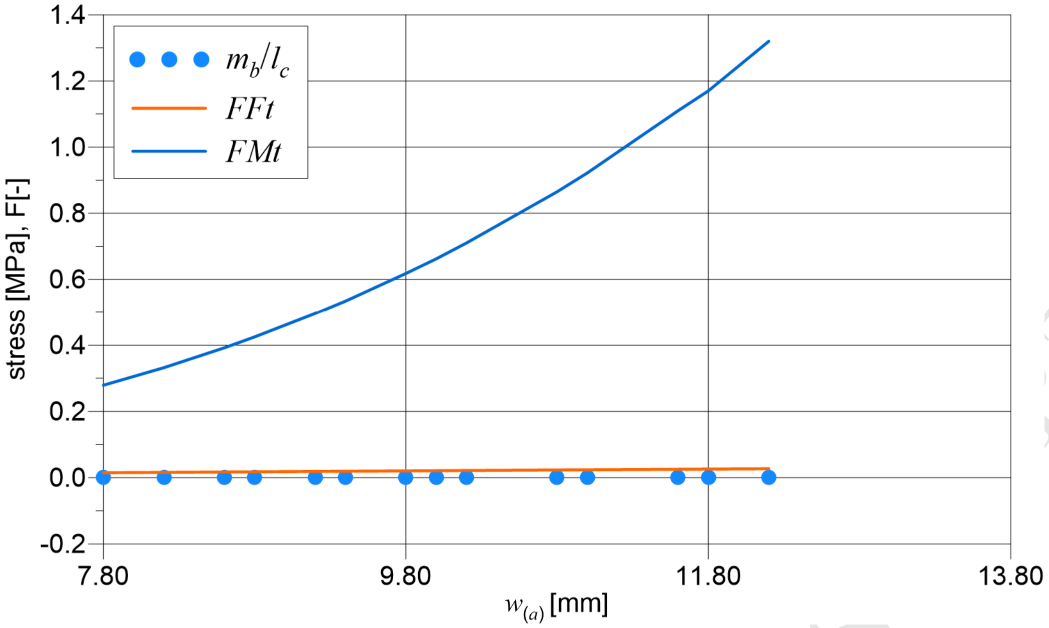

1.4
1.2
1.0
0.8
0.6
0.4
0.2
0.0
-0.2
stress [MPa], F[-]
7.80
9.80
11.80
13.80
$w_{(a)}$ [mm]
m_b/l_c
FFt
FMt

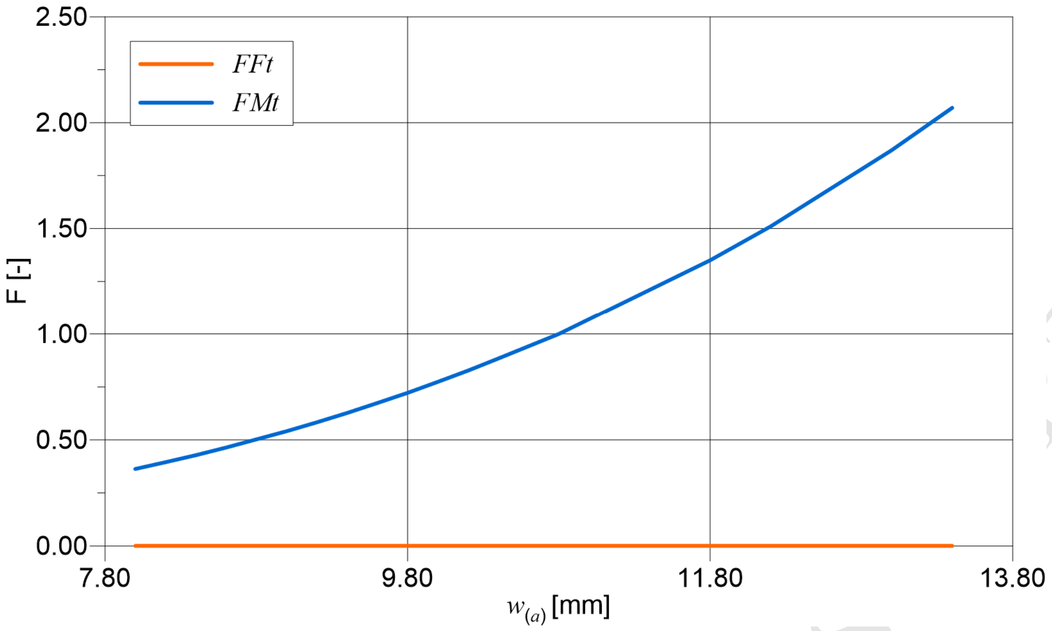
2.50
2.00
1.50
1.00
0.50
0.00
F [-]
7.80
9.80
11.80
13.80
$w_{(a)}$ [mm]
FFt
FMt

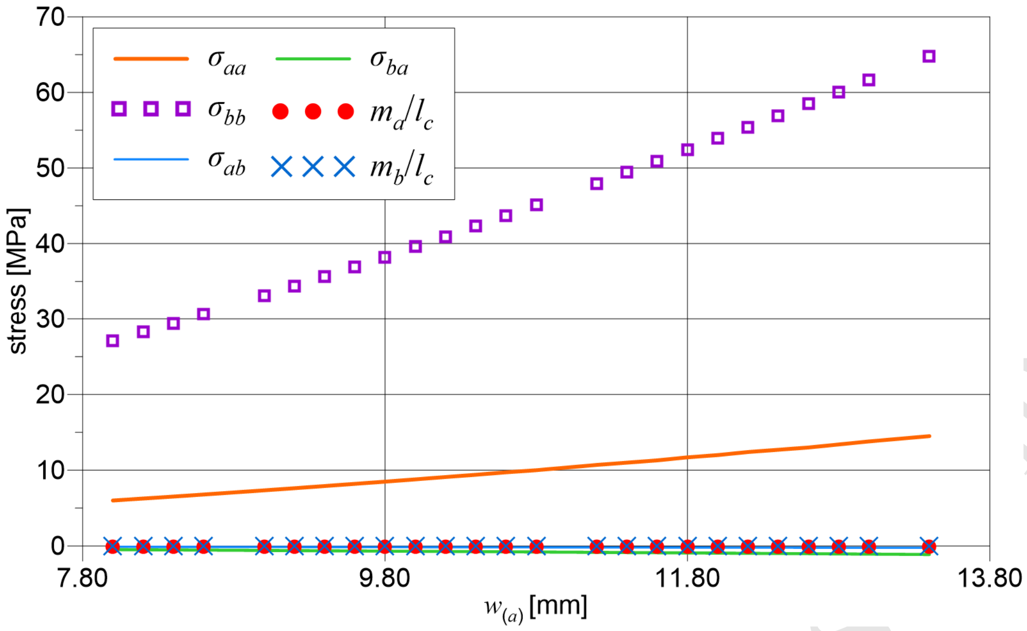
70
60
50
40
30
20
10
0
stress [MPa]
7.80
9.80
11.80
13.80
$w_{(a)}$ [mm]
σ_{aa}
σ_{ba}
σ_{bb}
m_d/l_c
σ_{ab}
m_b/l_c

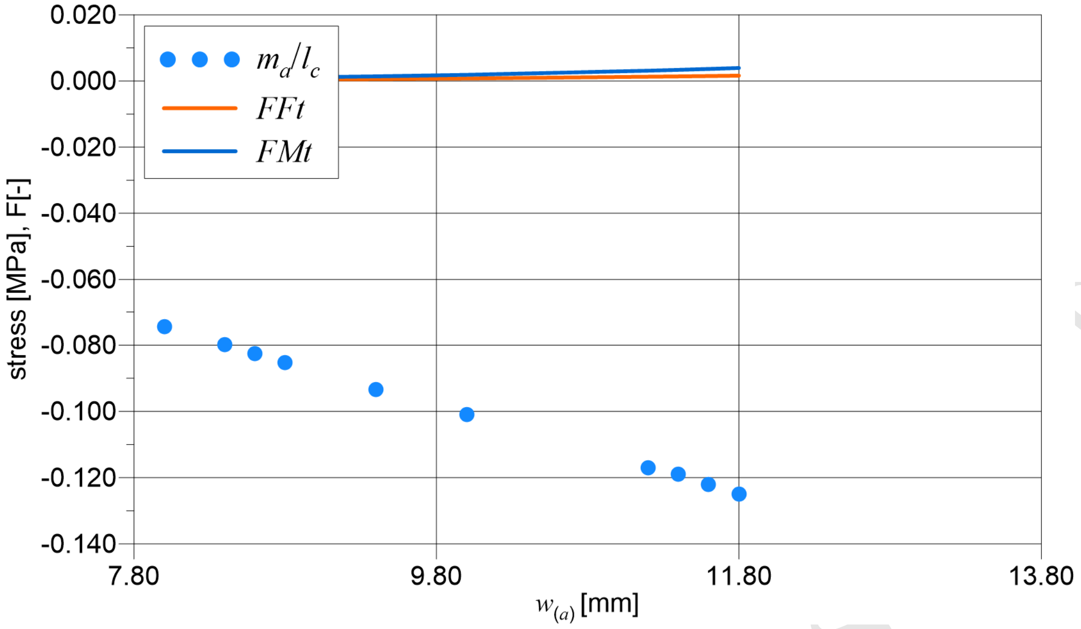
0.020
0.000
-0.020
-0.040
-0.060
-0.080
-0.100
-0.120
-0.140
stress [MPa], F[-]
7.80
9.80
11.80
13.80
$w_{(a)}$ [mm]
m_d/l_c
FFt
FMt

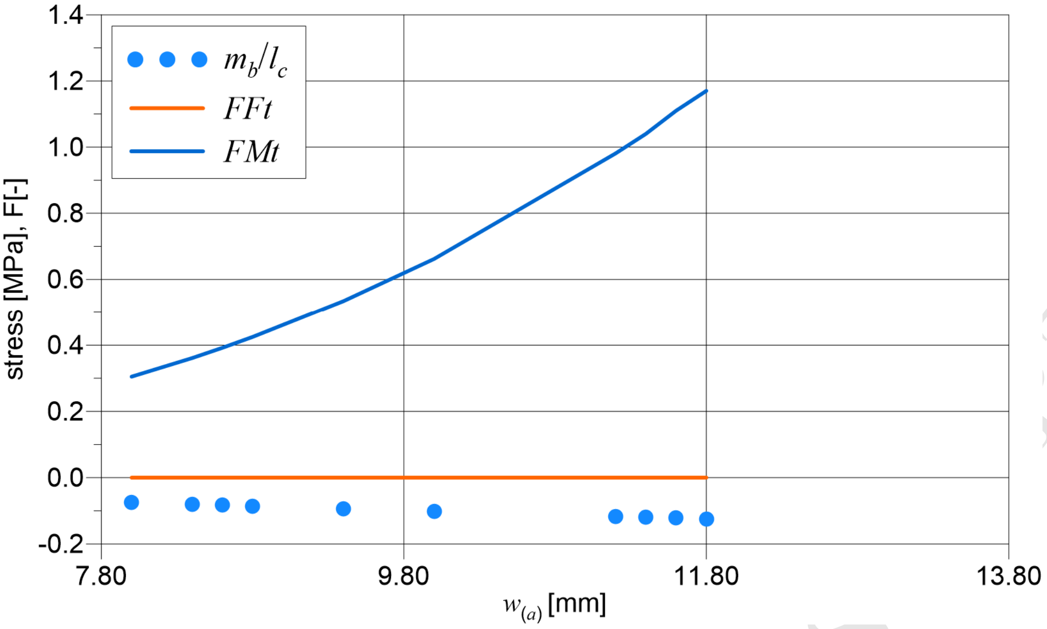
1.4
1.2
1.0
0.8
0.6
0.4
0.2
0.0
-0.2
stress [MPa], F[-]
m_b/l_c
FFt
FMt
7.80
9.80
11.80
13.80
$w_{(a)}$ [mm]

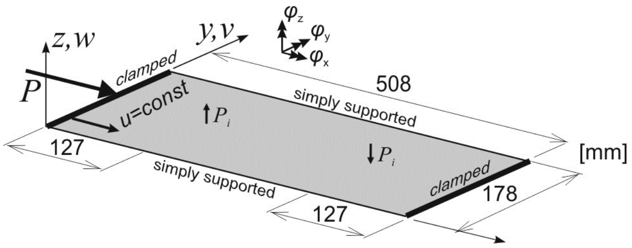
z,w
y,v
φz
φy
φx
P
clamped
u=const
Pi
508
simply supported
Pi
[mm]
127
simply supported
127
clamped
178

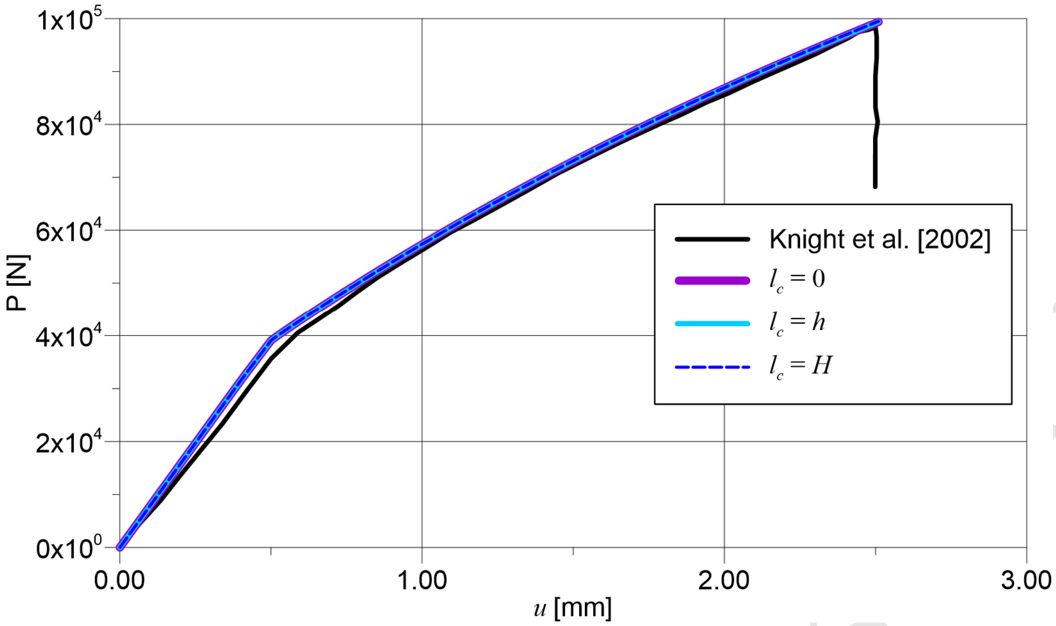
1x10^5
8x10^4
6x10^4
4x10^4
2x10^4
0x10^0
P [N]
0.00
1.00
2.00
3.00
u [mm]
Knight et al. [2002]
$l_c = 0$
$l_c = h$
$l_c = H$

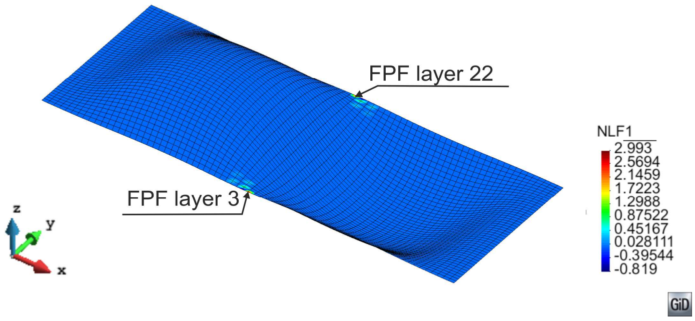
FPF layer 22
FPF layer 3
NLF1
2.993
2.5694
2.1459
1.7223
1.2988
0.87522
0.45167
0.028111
-0.39544
-0.819
z
y
x
GiD

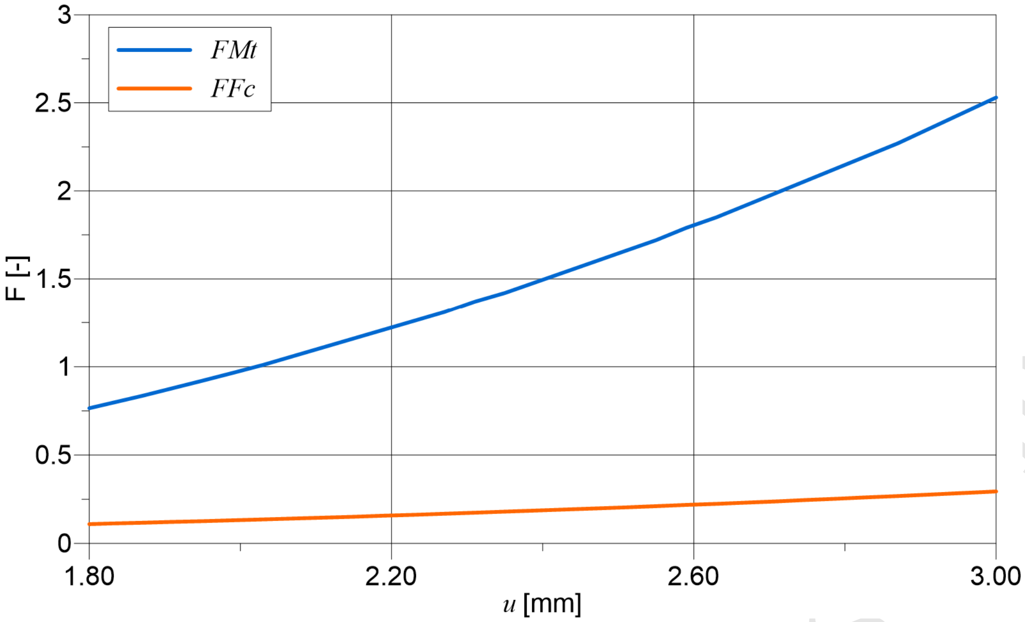
FMt
FFc
F [-]
3
2.5
2
1.5
1
0.5
0
1.80
2.20
2.60
3.00
u [mm]

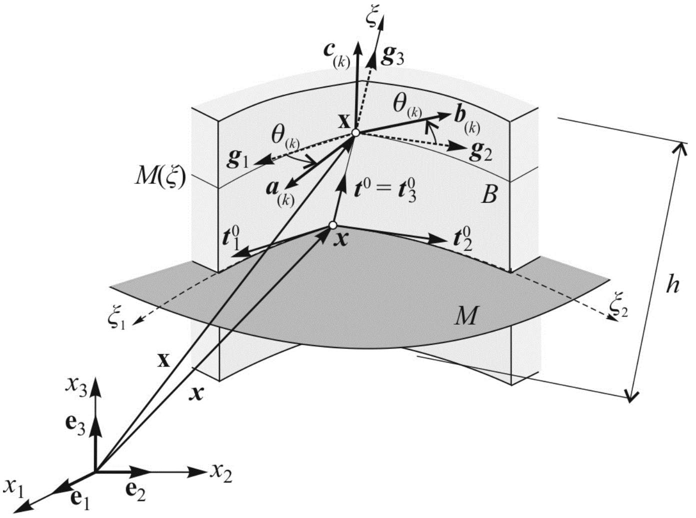
ξ
$\boldsymbol{c}_{(k)}$
$\boldsymbol{g}_3$
$\theta_{(k)}$
$\boldsymbol{b}_{(k)}$
$\mathbf{x}$
$\theta_{(k)}$
$\boldsymbol{g}_1$
$\boldsymbol{g}_2$
$M(\xi)$
$\boldsymbol{a}_{(k)}$
$\boldsymbol{t}^0 = \boldsymbol{t}_3^0$
B
$\boldsymbol{t}_1^0$
$\boldsymbol{x}$
$\boldsymbol{t}_2^0$
h
ξ_1
ξ_2
M
$\mathbf{x}$
$\boldsymbol{x}$
x_3
$\mathbf{e}_3$
x_1
$\mathbf{e}_1$
$\mathbf{e}_2$
x_2

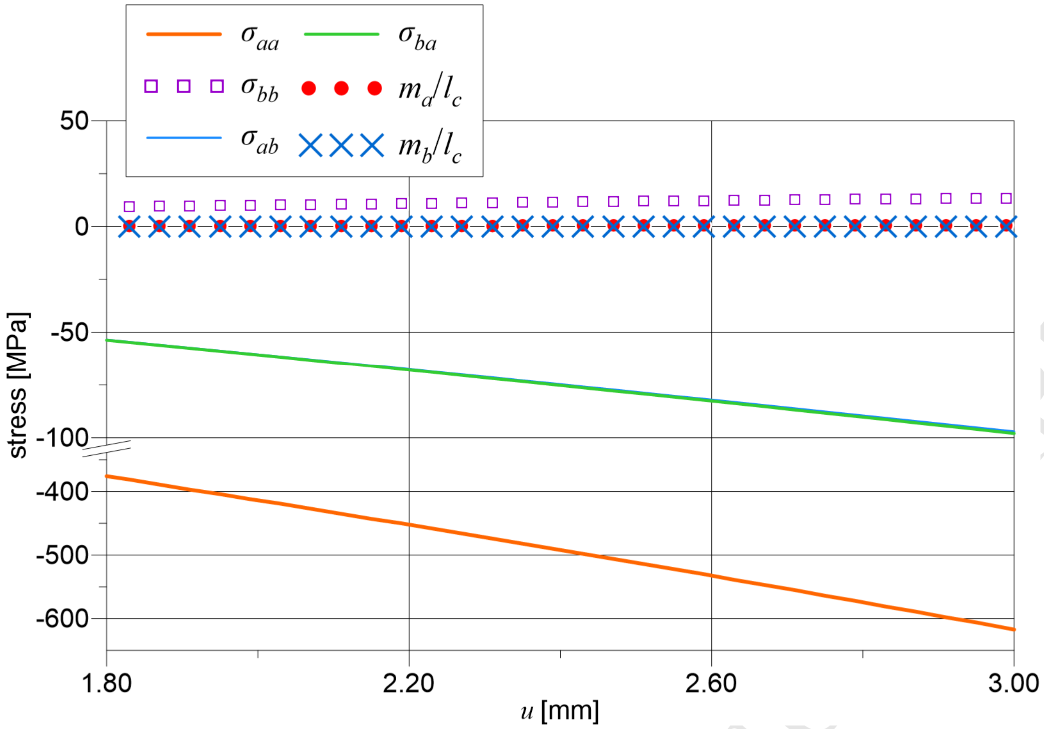
σ_{aa}
σ_{ba}
σ_{bb}
m_d/l_c
σ_{ab}
m_b/l_c
50
0
-50
-100
-400
-500
-600
stress [MPa]
1.80
2.20
2.60
3.00
u [mm]

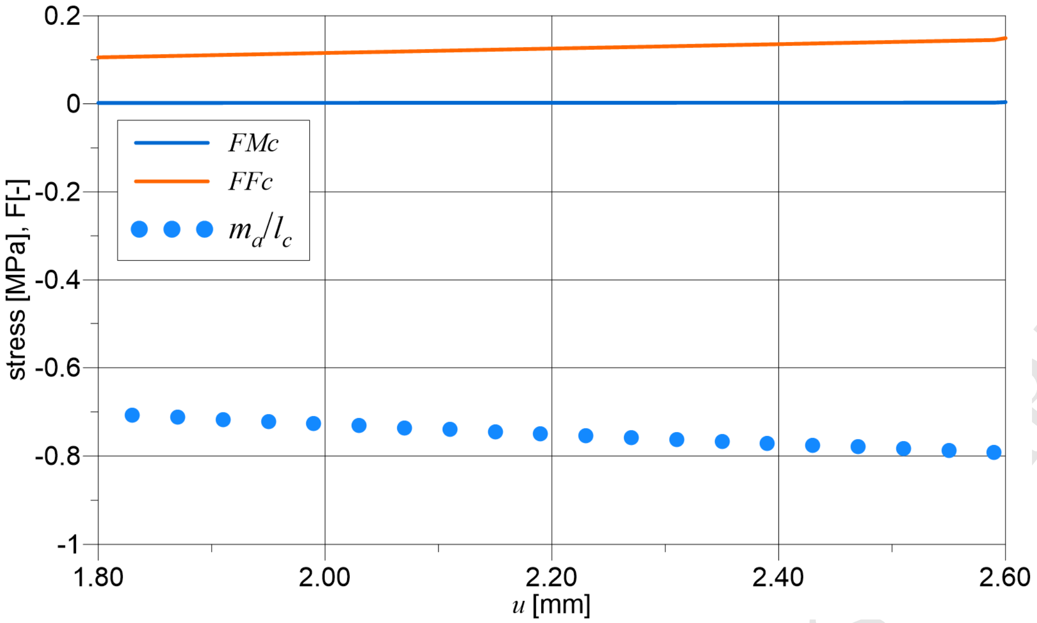
0.2
0
-0.2
-0.4
-0.6
-0.8
-1
stress [MPa], F[-]
1.80
2.00
2.20
2.40
2.60
u [mm]
FMc
FFc
m_d/l_c

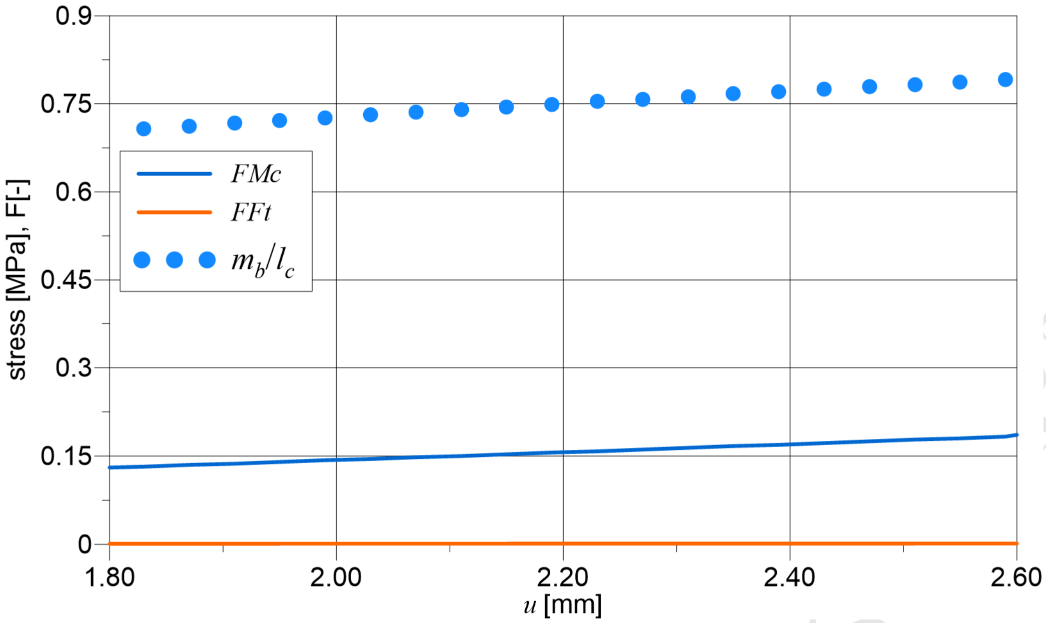
0.9
0.75
0.6
0.45
0.3
0.15
0
stress [MPa], F[-]
1.80
2.00
2.20
2.40
2.60
u [mm]
FMc
FFt
m_b/l_c

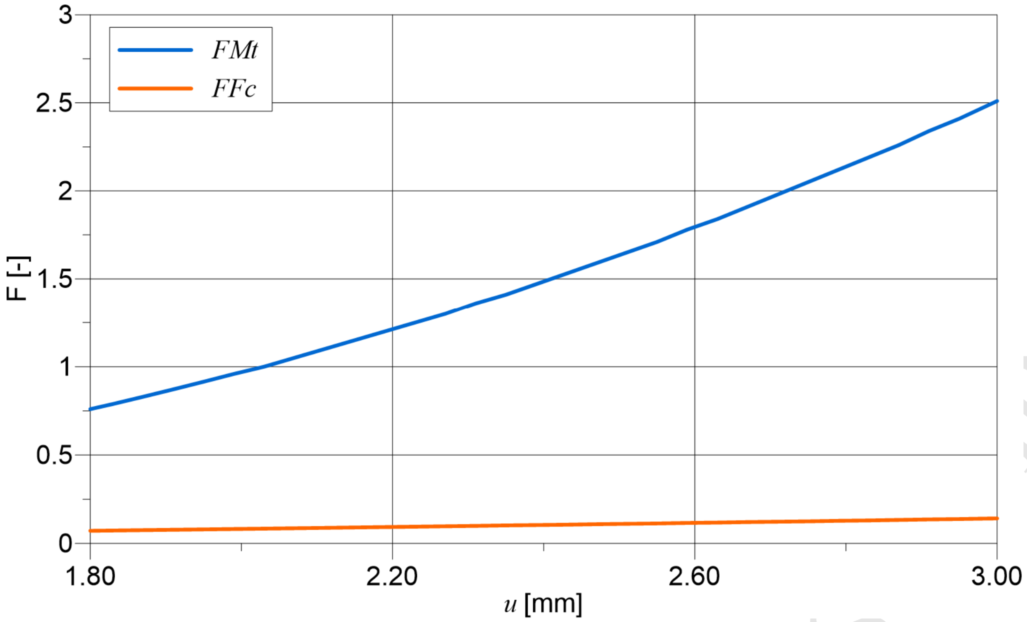
3
2.5
2
1.5
1
0.5
0
F [-]
1.80
2.20
2.60
3.00
u [mm]
FMt
FFc

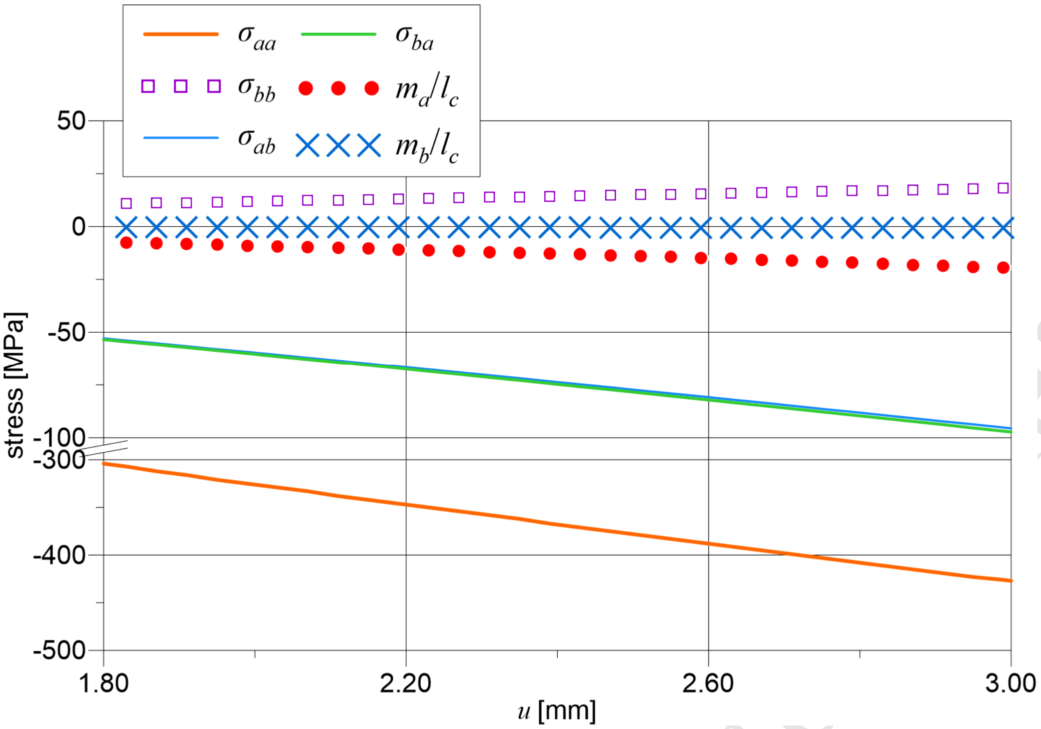
σ_{aa}
σ_{ba}
σ_{bb}
m_a/l_c
σ_{ab}
m_b/l_c
50
0
-50
-100
-300
-400
-500
stress [MPa]
1.80
2.20
2.60
3.00
u [mm]

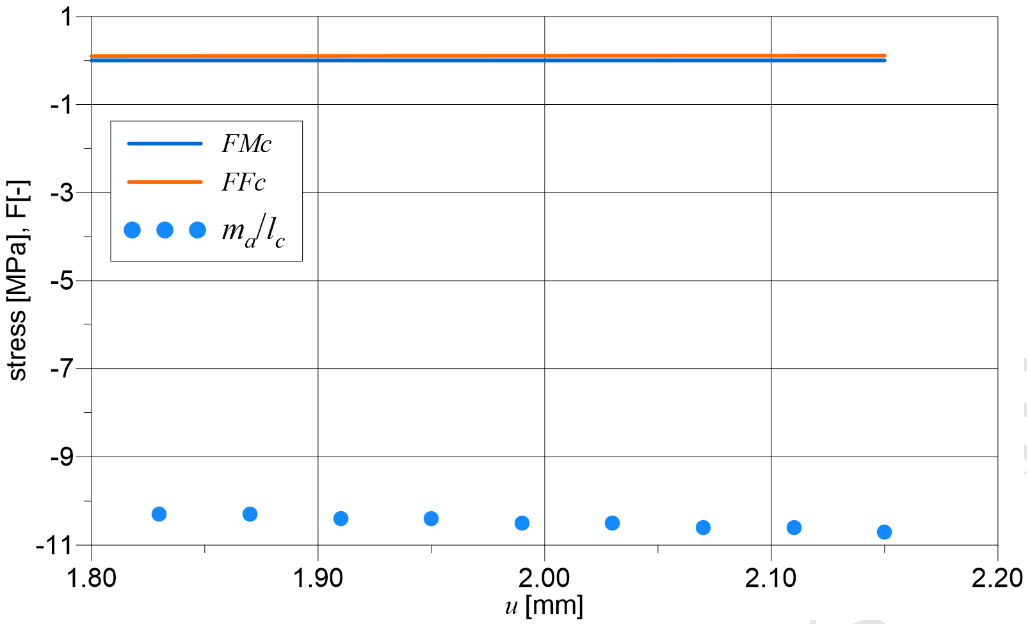
1
-1
-3
-5
-7
-9
-11
stress [MPa], F[-]
FMc
FFc
m_d/l_c
1.80
1.90
2.00
2.10
2.20
u [mm]

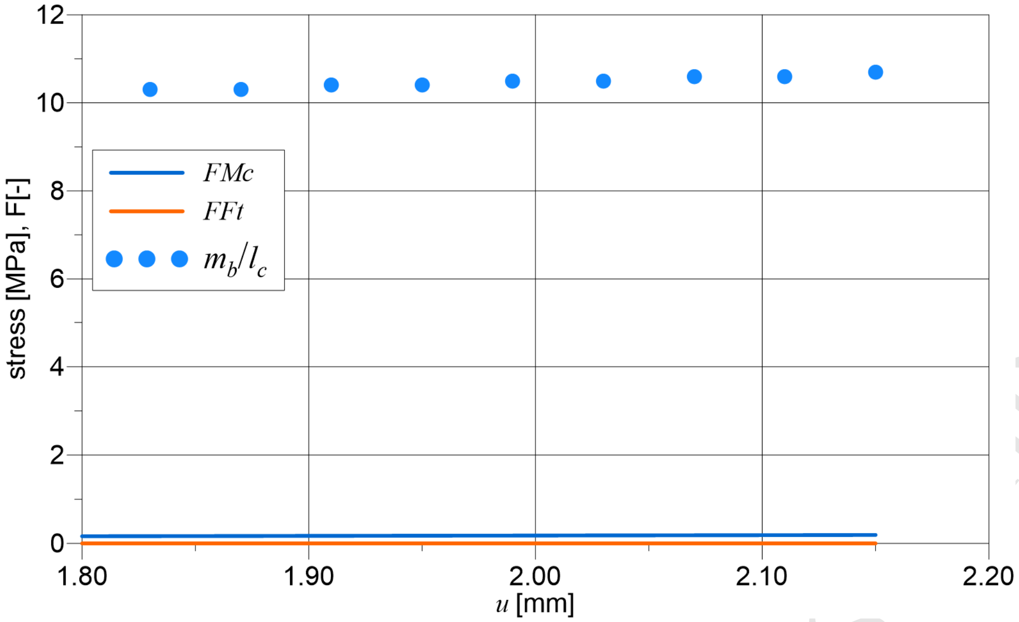
12
10
8
6
4
2
0
stress [MPa], F[-]
FMc
FFt
m_b/l_c
1.80
1.90
2.00
2.10
2.20
u [mm]

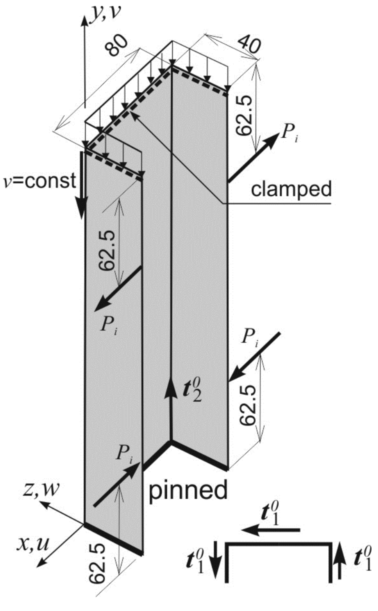
y,v
80
40
62.5
P_i
clamped
v=const
62.5
P_i
P_i
t_2^0
62.5
P_i
pinned
z,w
x,u
62.5
t_1^0
t_1^0
t_1^0

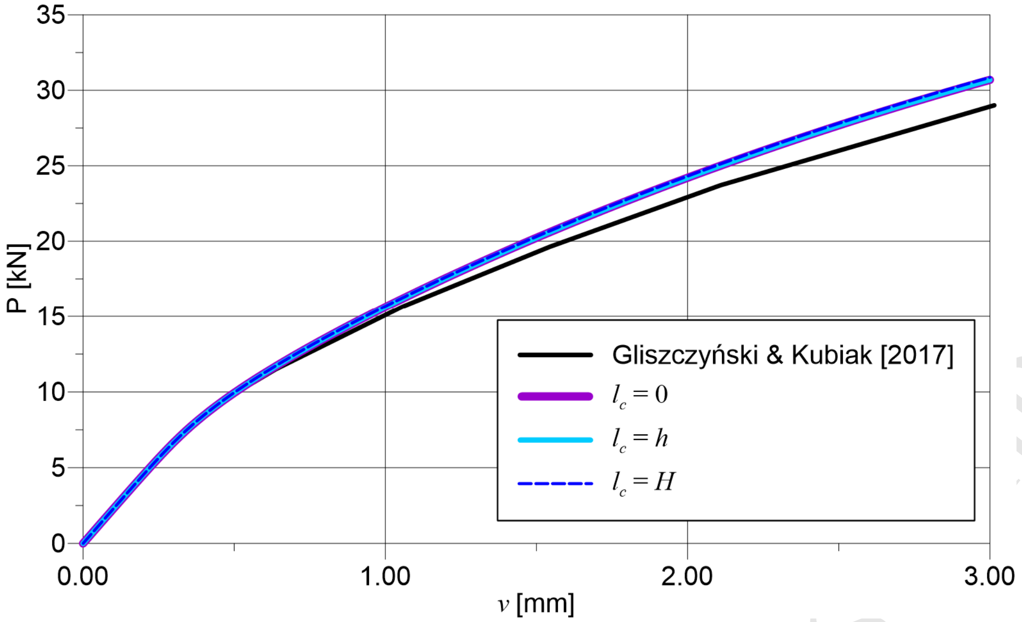
35
30
25
20
15
10
5
0
P [kN]
0.00
1.00
2.00
3.00
v [mm]
Gliszczyński & Kubiak [2017]
$l_c = 0$
$l_c = h$
$l_c = H$

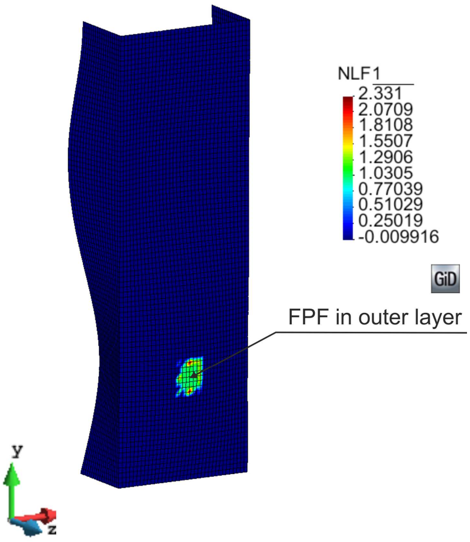
NLF1
2.331
2.0709
1.8108
1.5507
1.2906
1.0305
0.77039
0.51029
0.25019
-0.009916
GiD
FPF in outer layer
y
z

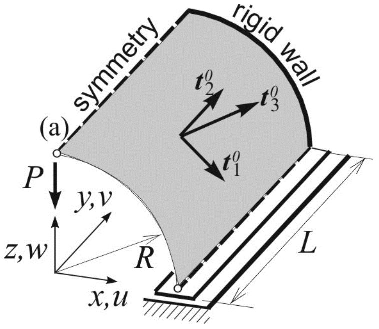
symmetry
rigid wall
(a)
t_2^0
t_3^0
t_1^0
P
y,v
z,w
R
L
x,u

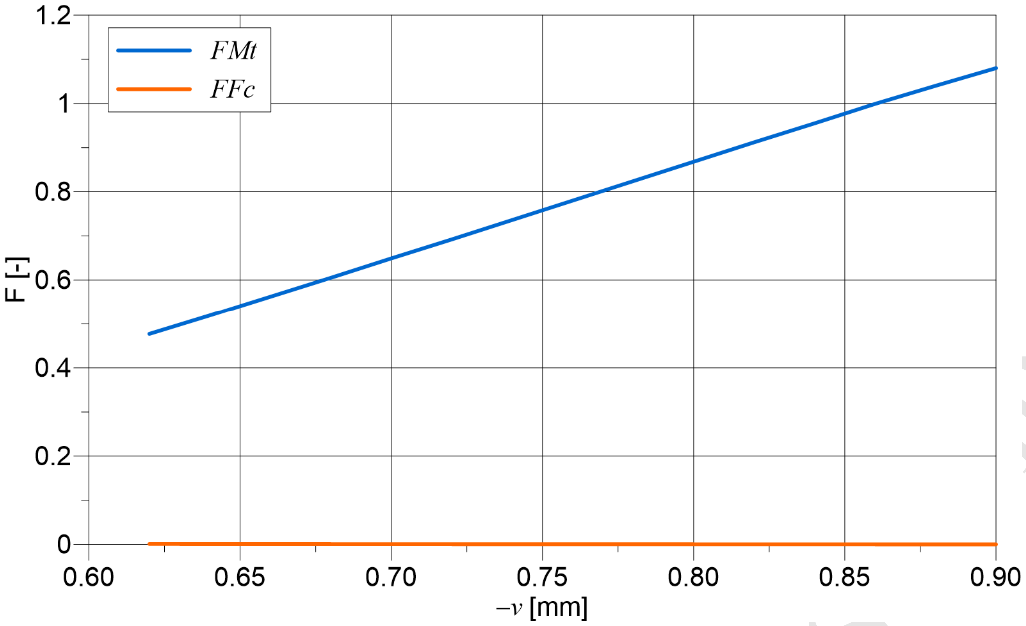
1.2
1
0.8
0.6
0.4
0.2
0
F [-]
0.60
0.65
0.70
0.75
0.80
0.85
0.90
$-v$ [mm]
FMt
FFc

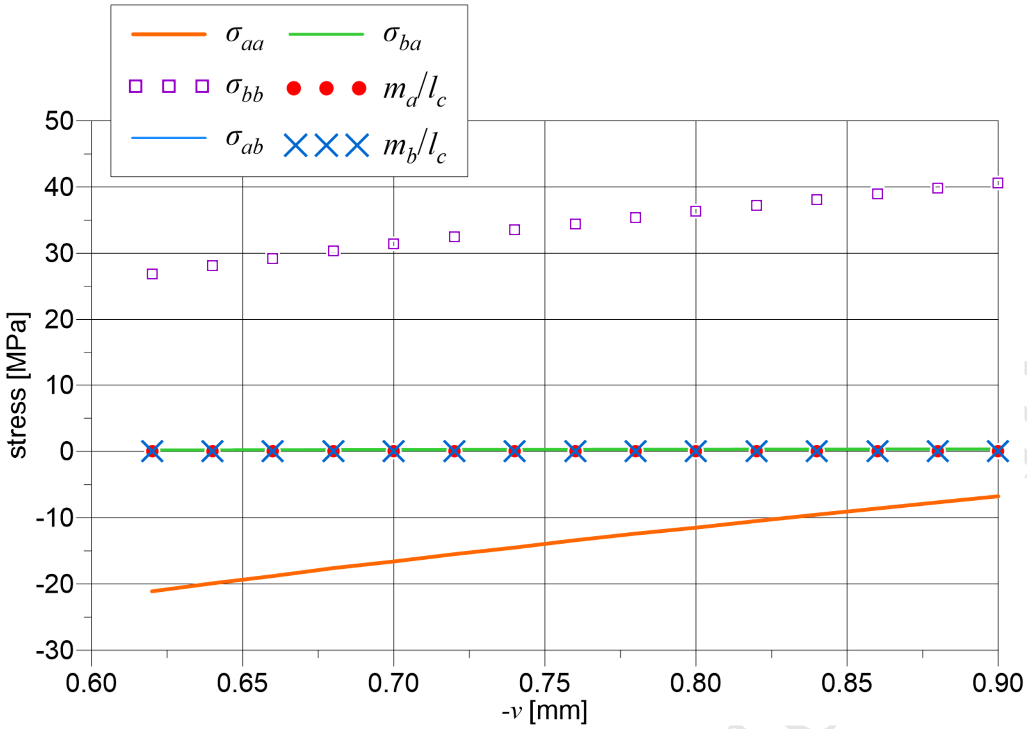
σ_{aa}
σ_{ba}
σ_{bb}
m_d/l_c
σ_{ab}
m_b/l_c
stress [MPa]
50
40
30
20
10
0
-10
-20
-30
0.60
0.65
0.70
0.75
0.80
0.85
0.90
-v [mm]

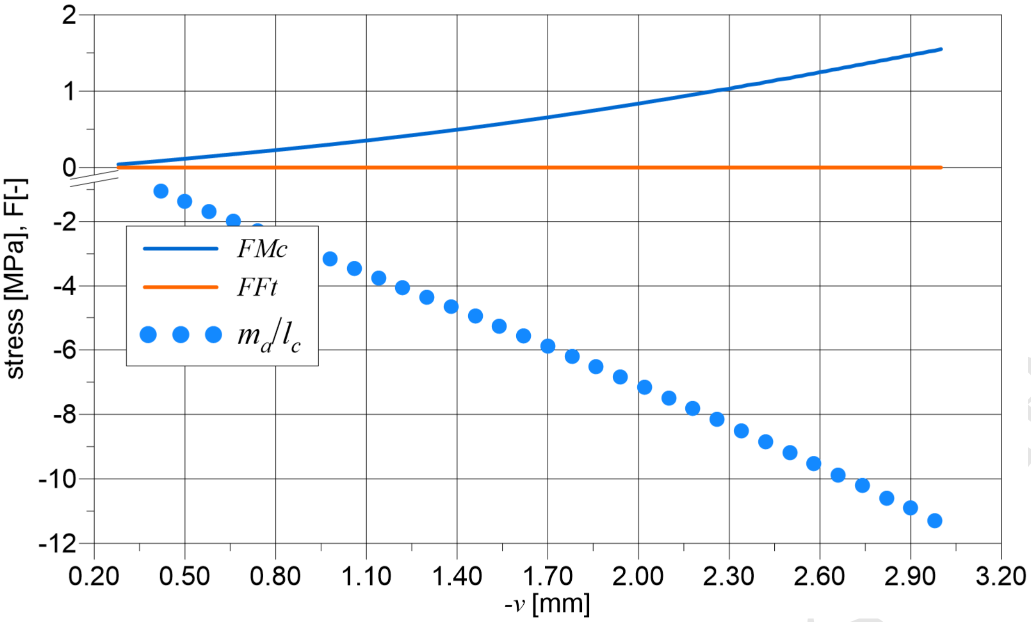
2
1
0
-2
-4
-6
-8
-10
-12
stress [MPa], F[-]
0.20
0.50
0.80
1.10
1.40
1.70
2.00
2.30
2.60
2.90
3.20
-v [mm]
FMc
FFt
m_d/l_c

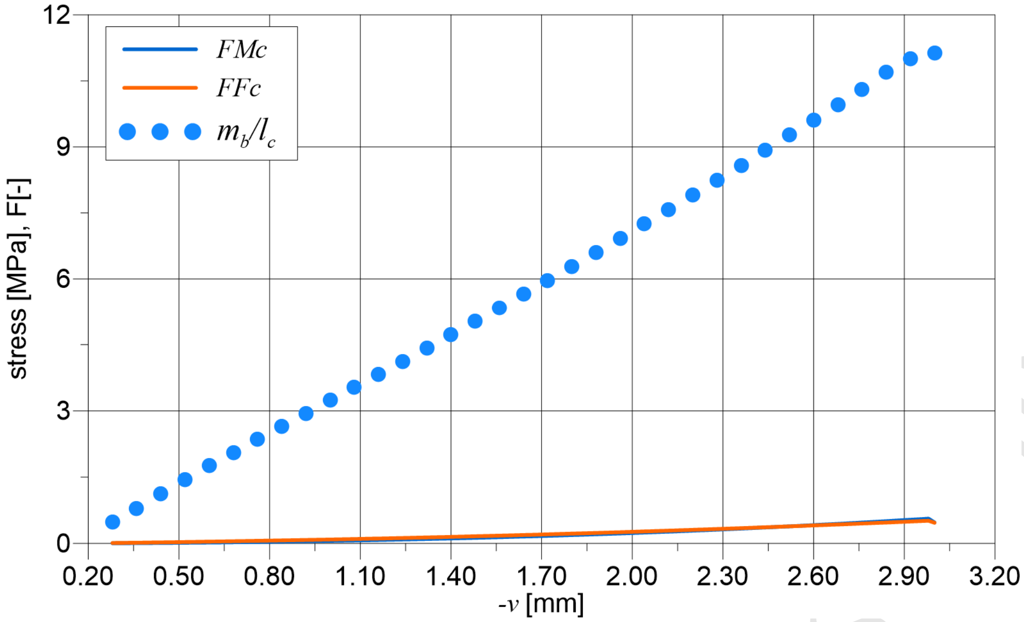
12
9
6
3
0
stress [MPa], F[-]
0.20
0.50
0.80
1.10
1.40
1.70
2.00
2.30
2.60
2.90
3.20
-v [mm]
FMc
FFc
m_b/l_c

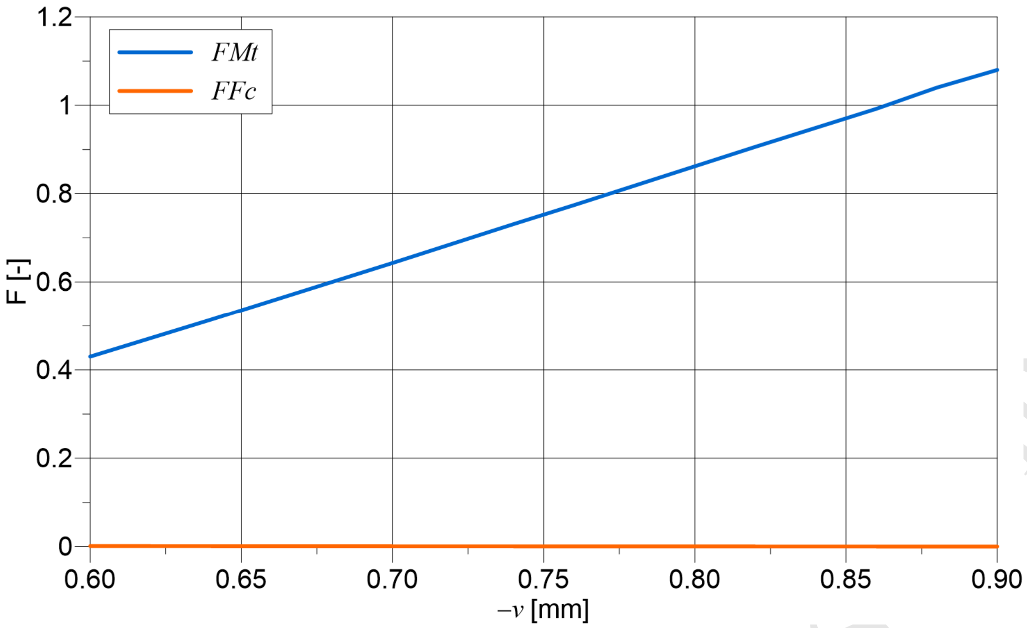
FMt
FFc
F [-]
1.2
1
0.8
0.6
0.4
0.2
0
0.60
0.65
0.70
0.75
0.80
0.85
0.90
$-v$ [mm]

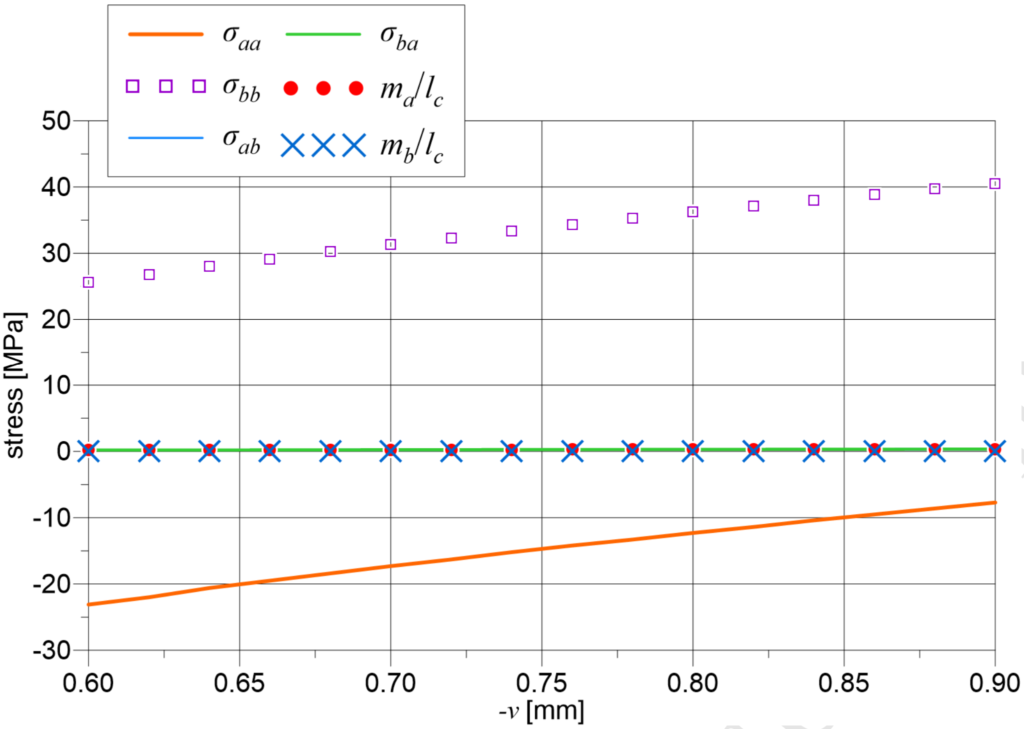
σ_{aa}
σ_{ba}
σ_{bb}
m_d/l_c
σ_{ab}
m_b/l_c
50
40
30
20
10
0
-10
-20
-30
stress [MPa]
0.60
0.65
0.70
0.75
0.80
0.85
0.90
-v [mm]

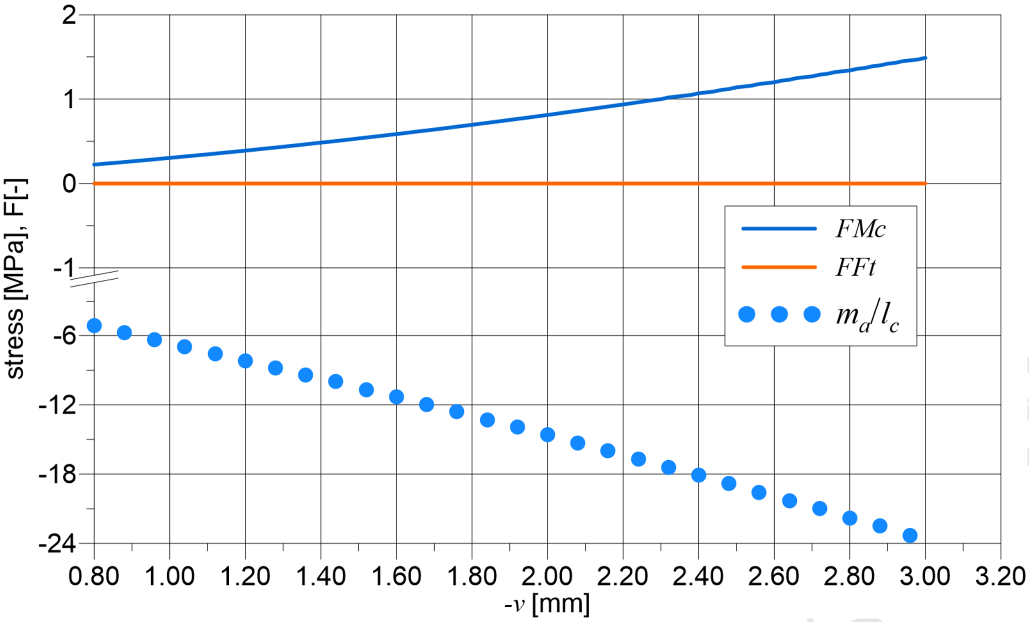
2
1
0
-1
-6
-12
-18
-24
stress [MPa], F[-]
0.80
1.00
1.20
1.40
1.60
1.80
2.00
2.20
2.40
2.60
2.80
3.00
3.20
-v [mm]
FMc
FFt
m_d/l_c

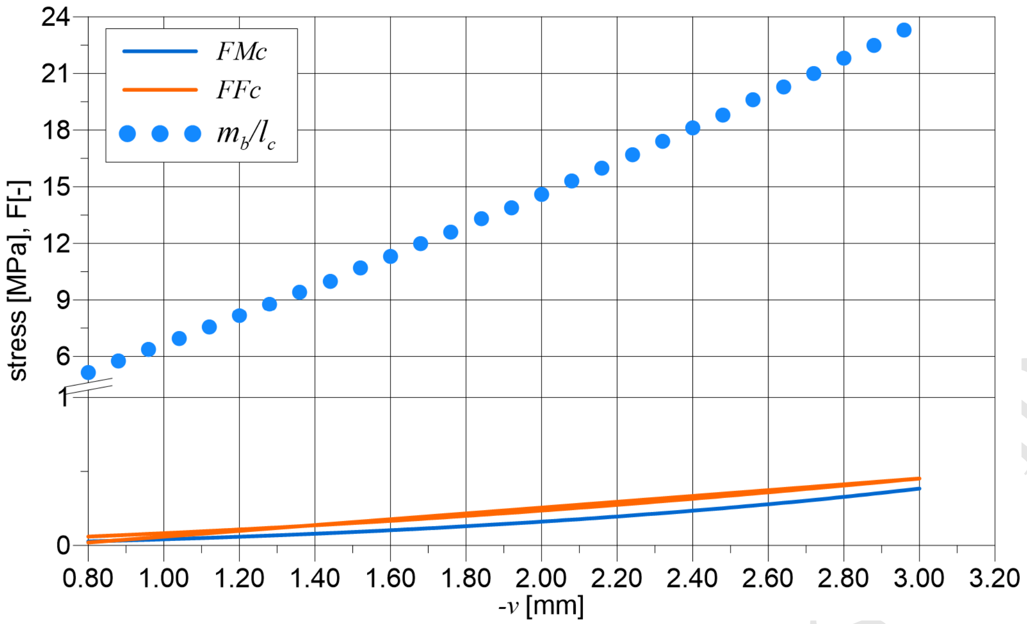
FMc
FFc
m_b/l_c
stress [MPa], F[-]
24
21
18
15
12
9
6
1
0
0.80
1.00
1.20
1.40
1.60
1.80
2.00
2.20
2.40
2.60
2.80
3.00
3.20
-v [mm]

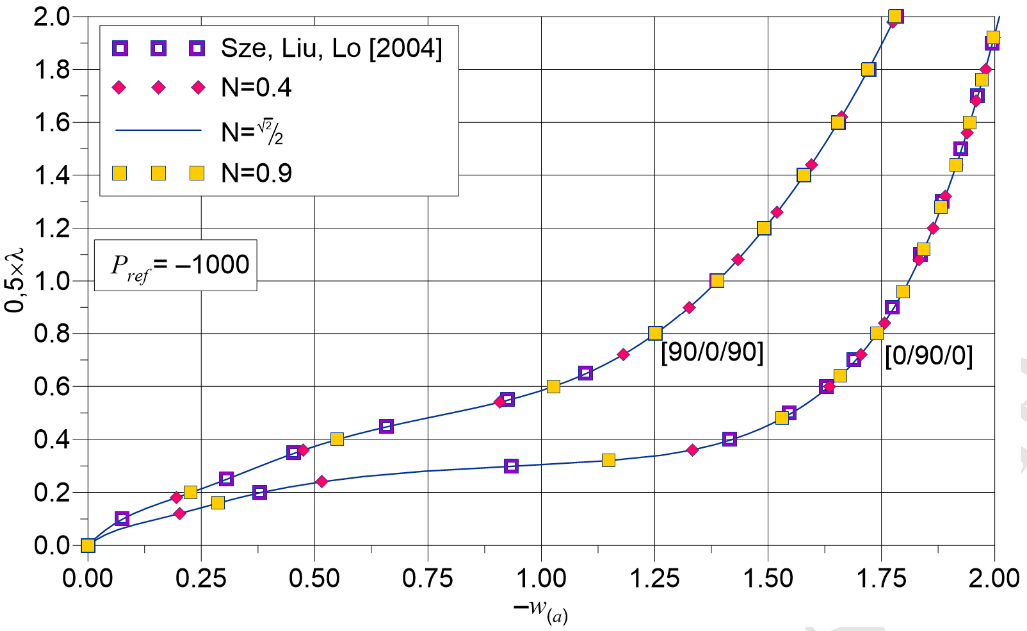
Sze, Liu, Lo [2004]
N=0.4
N=$\sqrt{2}/2$
N=0.9
P_{ref}= –1000
[90/0/90]
[0/90/0]
0,5×λ
–$w_{(a)}$
0.0
0.2
0.4
0.6
0.8
1.0
1.2
1.4
1.6
1.8
2.0
0.00
0.25
0.50
0.75
1.00
1.25
1.50
1.75
2.00

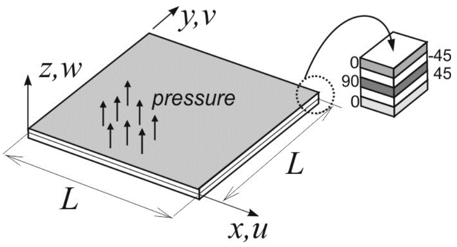
y,v
z,w
pressure
L
L
x,u
0
90
0
-45
45

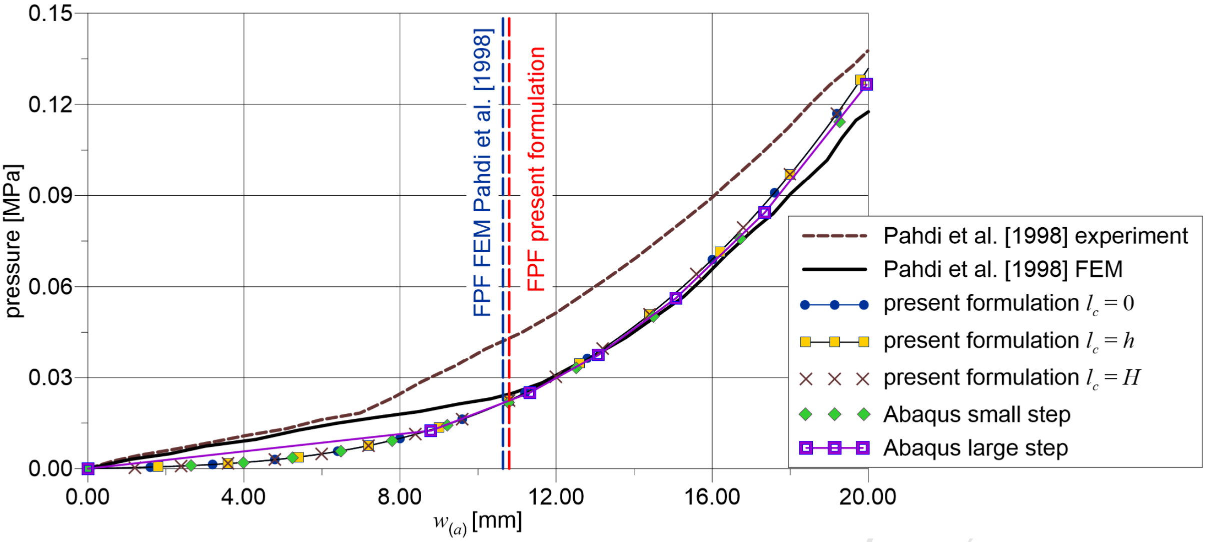

pressure [MPa]
0.15
0.12
0.09
0.06
0.03
0.00
0.00
4.00
8.00
12.00
16.00
20.00
$w_{(a)}$ [mm]
FPF FEM Pahdi et al. [1998]
FPF present formulation
Pahdi et al. [1998] experiment
Pahdi et al. [1998] FEM
present formulation $l_c = 0$
present formulation $l_c = h$
present formulation $l_c = H$
Abaqus small step
Abaqus large step

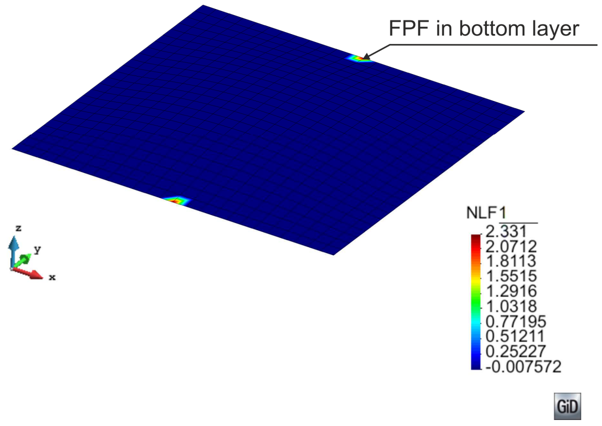
FPF in bottom layer
z
y
x
NLF1
2.331
2.0712
1.8113
1.5515
1.2916
1.0318
0.77195
0.51211
0.25227
-0.007572
GiD

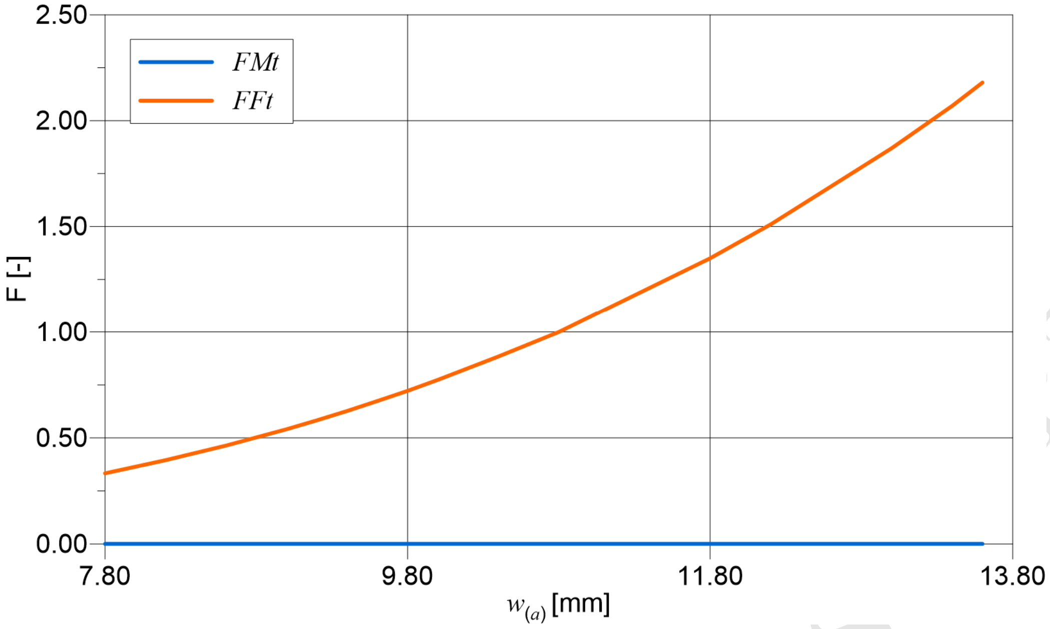
2.50
2.00
1.50
1.00
0.50
0.00
F [-]
7.80
9.80
11.80
13.80
$w_{(a)}$ [mm]
FMt
FFt

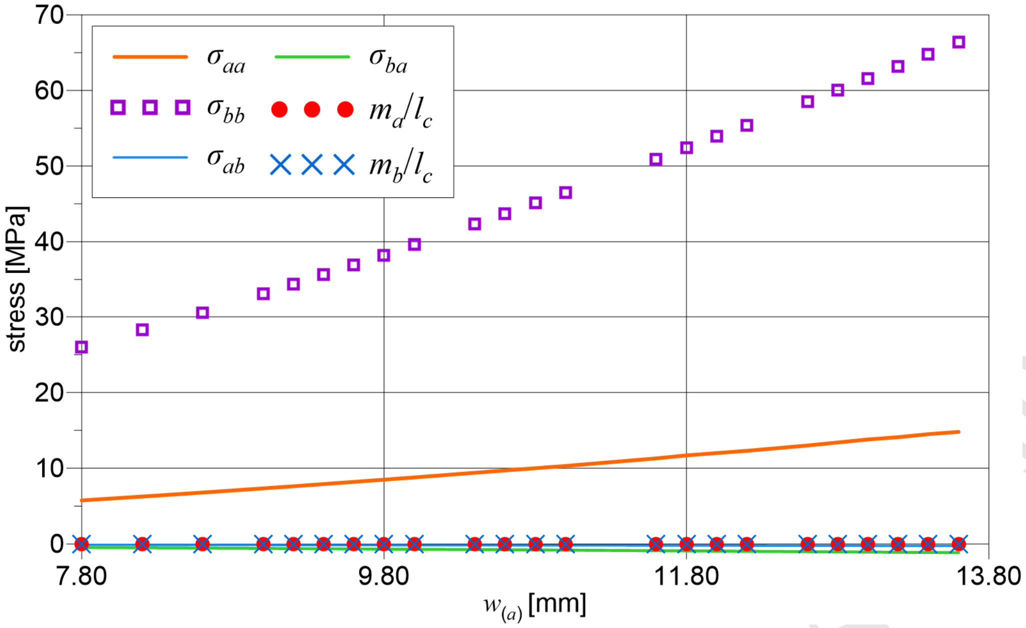
70
60
50
40
30
20
10
0
stress [MPa]
7.80
9.80
11.80
13.80
$w_{(a)}$ [mm]
σ_{aa}
σ_{ba}
σ_{bb}
m_d/l_c
σ_{ab}
m_b/l_c